

Simulation of Cooling Behavior and Microstructure Development of PM Steels

by

Amir Malakizadi

Diploma work No. 42/2010

at Department of Materials and Manufacturing Technology
CHALMERS UNIVERSITY OF TECHNOLOGY
Gothenburg, Sweden

Diploma work in the Master programme Advanced Engineering Materials

Performed at: Chalmers University of Technology
Department of Materials and Manufacturing Technology
SE-41296 Gothenburg, Sweden

Supervisor: Sepehr Hatami
Chalmers University of Technology
Department of Materials and Manufacturing Technology
SE-41296 Gothenburg, Sweden

Examiner: Prof. Lars Nyborg
Department of Materials and Manufacturing Technology
Chalmers University of Technology
SE-412 96 Gothenburg, Sweden

Simulation of Cooling Behavior and Microstructure Development of PM Steels

AMIR MALAKIZADI

© AMIR MALAKIZADI, 2010.

Diploma work no 42/2010
Department of Materials and Manufacturing Technology
Chalmers University of Technology
SE-412 96 Gothenburg
Sweden
Telephone + 46 (0)31-772 1000

[CHALMERS Reproservice]
Gothenburg, Sweden 2010

To my lovely mum and dad

ABSTRACT:

In recent years, growing demand for greater mechanical properties of PM steel components with competitive fabrication cost has led to enormous innovation in different aspects of PM industry. Recent research has focused on introducing new alloying systems, different furnace atmospheres and combining sintering and post sintering processes for more hardenable powder metallurgy (PM) steels. By elimination of any secondary operation such as quench-hardening and instead by introducing the hardening treatment right after sintering, fabrication cost is reduced by far. Sinter-hardening is a result of research conducted along this line. In this process, it is possible to manufacture sintered parts with a martensitic-bainitic microstructure by applying sufficient cooling rates (1-10°C/s depending on composition) directly after sintering. In addition, alloying elements such as Cr, Mo and Mn are usually added to the Fe-based powder to enhance the hardenability of the material.

In this thesis, the cooling response of prealloyed steel powder during the sinter-hardening process has been investigated by means of Finite Element Method (FEM). An axi-symmetric FE model has been developed using MATLAB to predict the cooling response, considering the effects of nonlinear boundary conditions, latent heat of phase transformation and nonlinear thermal properties. The code was verified in two steps, firstly, by means of ANSYS commercial code and later by making a comparison between the results of the present FE simulation and the works done by previous researchers. Finally, the method was applied to simulate the cooling response and microstructural development of two prealloyed Cr-Mo steel powder grades; Astaloy CrL+0.6%C and Astaloy CrL+0.8%C.

Keywords: Sinter-hardening, PM steel, FEM simulation, Phase transformation

TABLE OF CONTENTS

| | |
|--|----|
| 1. OBJECTIVES:..... | 1 |
| 2. BACKGROUND | 1 |
| 2.1 Heat treatment of PM steels- Sinter hardening process | 1 |
| 2.2 Alloying methods - Hardenability of PM steels | 1 |
| 2.2.1 The Grossman test | 3 |
| 2.2.2 The Jominy test | 3 |
| 2.3 Phase transformation in steels | 4 |
| 2.3.1 Ferritic and pearlitic transformations | 5 |
| 2.3.2 Martensitic transformation..... | 5 |
| 2.3.2.1 Thermodynamics aspects of martensitic transformation in steels | 6 |
| 2.3.2.2 Effects of alloying elements | 7 |
| 2.3.2.3 Effect of grain size | 9 |
| 2.3.2.4 Surface effects on martensite start temperature | 10 |
| 2.3.2.5 Kinetics of martensitic transformation in steels | 10 |
| 2.3.3 Bainitic transformation | 11 |
| 2.3.3.1 Kinetics of bainitic transformation | 12 |
| 2.3.3.2 Effect of austenite grain size | 12 |
| 2.4 Kinetic models for diffusive transformations | 13 |
| 2.4.1 Johnson–Mehl–Avrami–Kolmogorov (JMAK) model..... | 13 |
| 2.4.2 Austin and Rickett (AR) model..... | 14 |
| 2.4.3 Kirkaldy equations | 15 |
| 2.4.4 Scheil’s principle | 15 |
| 2.4.5 Effects of porosity on the kinetics of transformations..... | 16 |
| 2.5 Constitutive equation and finite element formulation..... | 17 |
| 2.5.1 Constitutive equation | 17 |
| 2.5.2 FE Formulation | 18 |
| 2.5.3 Incorporating the phase transformation terms | 20 |
| 2.5.4 Incorporating the effects of porosity in the developed FE model | 23 |
| 3. RESULTS | 25 |
| 3.1 Verification of the FE code excluding the phase transformation effects | 25 |
| 3.2 Verification of the FE code including the phase transformation effects | 27 |
| 3.3 Cooling response in Astaloy CrL+0.6%C and Astaloy CrL+0.8%C | 32 |
| 4. DISCUSSION | 36 |
| 4.1 Verification routine | 36 |
| 4.2 FE modeling of cooling response in Astaloy CrL PM Steel | 36 |
| 4.3 Considerations for PM steels | 37 |
| 5. CONCLUSIONS | 39 |
| 6. ACKNOWLEDGEMENT | 40 |
| 7. REFERENCES..... | 41 |

1. OBJECTIVES:

The aim of this project is:

1. To develop a 2D axi-symmetric FE code to simulate the cooling response in components with axial symmetry, such as rings and cylinders
2. To predict the cooling rate of PM steel components during the sinter-hardening treatment
3. To predict the microstructure development when cooling from sintering temperature
4. To predict the sinter-hardening response of different materials and geometries

2. BACKGROUND:

2.1 Heat treatment of PM steels- Sinter hardening process

Generally, in order to obtain increased strength, hardness and wear resistance, ferrous PM components containing adequate amount of carbon and alloying elements may be heat treated to form bainitic/martensitic microstructure. The conventional heat treatment procedures can be applied to PM steels to achieve desirable mechanical properties. Quench-hardening followed by tempering treatment is a common practice in the PM industry. In this method, the sintered PM components are heated up to austenitizing temperature and quenched in agitated oil bath. The components are tempered after quenching, in order to partially regain the lost ductility (due to quenching). The other most frequent method is sinter-hardening which is applicable to PM steel grades with high hardenability. The term hardenability refers to the ability of a certain steel to form in-depth martensite when cooling from austenitizing temperature [1]. This term will be explained in detail later. In sinter-hardening process by applying high cooling rates, the component hardens when cooling from the sintering temperature and thus, the need for secondary heat treatment (i.e. quench-hardening) is eliminated. This method has some benefits over the quench-hardening process [2]. Due to less severe quenching, the components are less distorted, and consequently better dimensional control is attainable. Moreover, if tempering is needed, it is easier to apply such treatments on sinter-hardened steels. During oil quenching of PM steels, usually considerable amount of oil is trapped in the pores, which must be burnt off before tempering the material above 200°C. In addition, in case of using finishing processes such as plating, the sinter-hardening components does not need oil removal step [2].

2.2 Alloying methods - Hardenability of PM steels

The alloying elements added to the ferrous powder determine the processability of the PM steel grade in terms of compaction, sintering and post sintering treatments responses. In particular, the final mechanical properties of the PM components are directly influenced by amount of alloying elements in solution. There are four main alloying methods for ferrous materials, which is classified according to the manner that they are added to the base iron powder [2]:

- Admixed- certain amount of alloying elements are mixed with base iron powder and compacted within the die. Since the iron powder is unalloyed, the adverse effect of alloying elements on compressibility is the least using this alloying method. However, the microstructure of the material after sintering is highly heterogeneous, and there are some concerns about dusting during handling and compaction.
- Diffusion bonded- a mix of certain alloying elements and iron powder is hydrogen annealed at elevated temperature (generally 800 °C - 900 °C) to develop partial diffusion bonding between them [3]. The final microstructure is heterogeneous, due to chemical gradient

within the material; however, the compressibility is higher than the prealloyed powder grades.

- Prealloyed- alloying elements, except for carbon, are mixed in the molten state and then atomized to form alloyed powders. Due to uniform distribution of the alloying elements, the final microstructure is homogeneous. However, this alloying method results in lower compressibility due to solution hardening of the powder.
- Hybrid alloys- this method involves mixing elemental alloys with highly compressible prealloyed powders [4].

Generally, hardenability is defined as the distance below the quenched surface, where a specific hardness is achieved [4]. According to ASTM A255 standard, the hardenability depth can be determined as the distance below the quenched end where the value of hardness drops below 65 HRA. In other words, only those grades of steel, in which the formation of relatively soft phases (e.g. ferrite and pearlite) is retarded upon cooling from austenitic region, are considered hardenable. For any given steel there is a critical cooling rate at which the decomposition of austenite to ferrite, pearlite and bainite can be avoided during cooling. Carbon content, alloying elements and austenite grain size are all factors that determine this critical cooling rate. Fig. 1 shows the TTT (time temperature transformation) curves for 1060 steel (Fe-0.63% C-0.87 %Mn) and 4068 steel (Fe-0.68 %C-0.87 %Mn-0.24 %Mo) [5]. As can be seen, addition of a small amount of Mo, suppressed the pearlite nose to a significantly later time. This shift in TTT curve, make it possible to attain martensite during cooling from austenitic region for 4068 steel. It is worthy to note that these figures are illustrated here only to show the effects of alloying elements on hardenability, and under continues cooling condition, CCT curves are to be used to accurately predict the transformed phases. It should also be noted that only fractions of alloying elements in solid solution in austenite can contribute to the hardenability of the steel grade. Thus, among above alloying methods, prealloyed steel powders usually exhibit better hardenability. In general, two different experiments are more commonly used to evaluate the hardenability of steels, the Grossman test and the Jominy (quench) test.

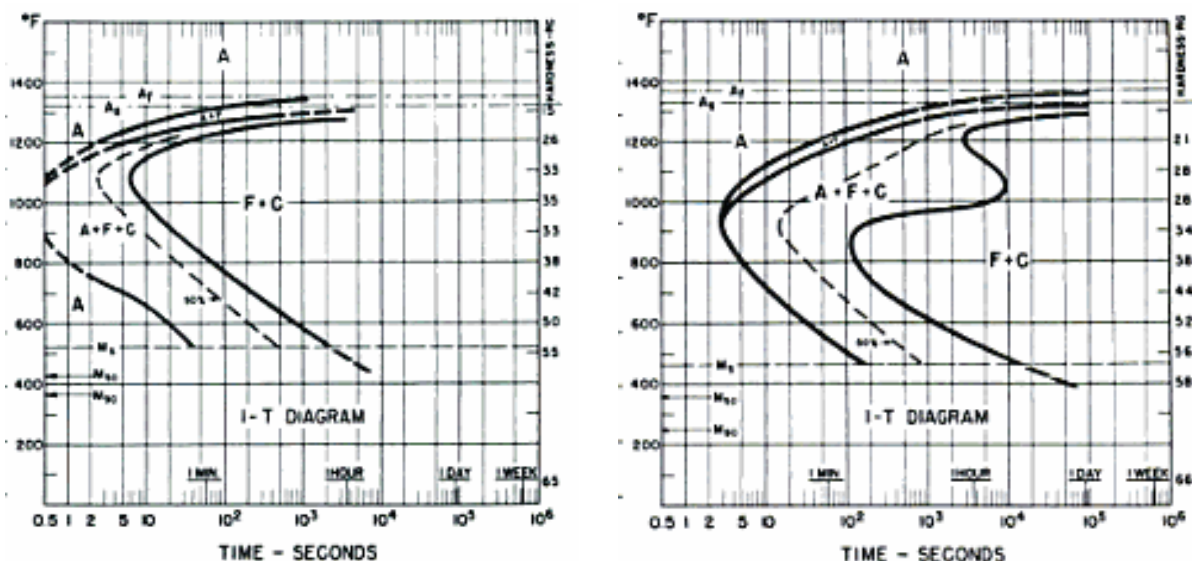


Fig.1: TTT diagram for a)1060, composition:0.63 %C-0.87%Mn (wt.%), austenitizing temperature 816 °C, grain size: ASTM 5-6 b) 4068, composition: 0.68 %C-0.87%Mn-0.24%Mo (wt.%), austenitized at 899 °C, grain size: ASTM 7-8 [5]

2.2.1 The Grossman test

In Grossman test, the hardenability is defined in terms of the ideal critical diameter (D_I), which is the diameter of a cylinder that can form 50% martensite at its center, when cooled with an ideal quenchant. The term ideal quenchant implies that the temperature of the cooling media remains unchanged during the quenching process. The ideal critical diameter (D_I) varies with steel composition and austenite grain size. To evaluate the effect of alloying elements and grain size on hardenability, Grossman and co-workers defined a base ideal diameter (D_0) which only depends on carbon content and grain size. Later, the effect of alloying elements is introduced by means of multiplying factors;

$$D_I = D_0 \times f_1 \times f_2 \times f_3 \times \dots \quad (1)$$

Fig.2a shows the dependence of the base ideal diameter on carbon content and ASTM grain size. Multiplying factors for each element can be obtained from Fig.2b. As can be seen, Cr, Mn and Mo improve hardenability of steels more effectively than Ni and Si.

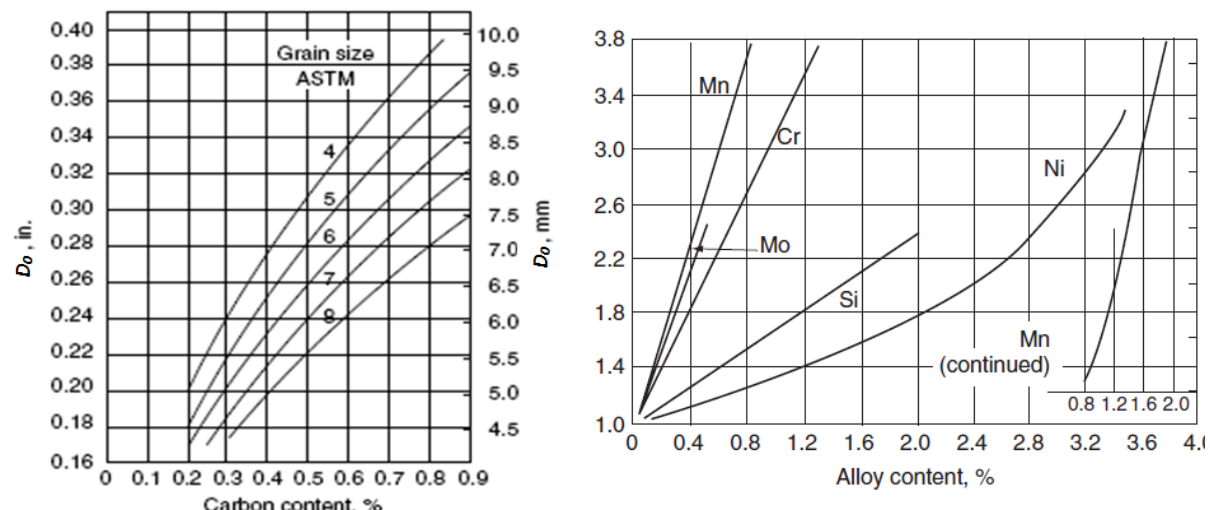


Fig.2: a) effect of carbon content and ASTM grain size on D_0 , b) multiplying factors for alloying element (after Totten [1] with some modification)

2.2.2 The Jominy test

The Jominy test involves end-quenching of a standardized cylindrical specimen. After quenching, the cylinder bar is ground to make two opposite parallel flat surfaces. Then, the hardness values are measured along the bar at 1/16 inch intervals from quenched end. Fig.3a shows an illustrative Jominy hardenability curve. The test is covered by ASTM A255 standard. Fig.3b shows the dimension of the Jominy test bar and end-quenching condition. According to ASTM A255 standard, a cylindrical bar with specific dimensions ($\varnothing 25\text{mm} \times 100\text{mm}$) is heated up to austenitizing temperature and soaked for 30 min. it is then placed at a holding fixture and quenched from the lower end by means of a jet of water under a certain condition, shown in Fig.3a. Different cooling rates at different distances from the quenched end ensure that the various phases can be formed along the bar. Depending on the steel composition and the grain size, martensite will most likely form at the quenched end, and moving away from the quench end, gradually bainite, ferrite and/or pearlite may form. Consequently, the hardness will gradually decrease as we move further away from the quenched end which is martensitic.

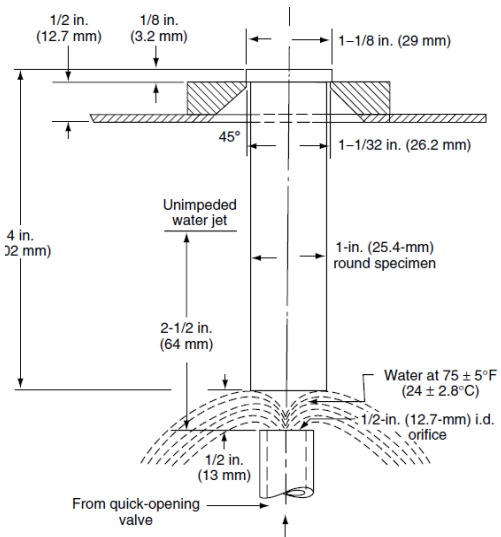
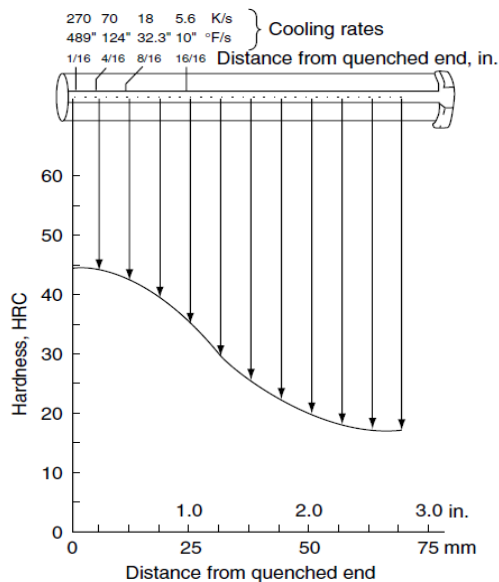


Fig. 3 a) illustrative Jominy hardenability curve b) Jominy specimen and test conditions [1]

2.3 Phase transformation in steels

In general, steel refers to an iron-carbon alloy, which may contain up to 2 wt.% C. Although carbon is the most common element, a group of alloying elements such as Mn, Si, Cr, Mo and Ni may also be added to steels to obtain desired properties. Obviously, these elements need to be added to the iron base in molten state, generally at temperature above 1600 °C. When cooling from liquid state, different phase transformations can take place, as shown in Fig.4. The first phase transformation is from liquid \rightarrow δ -ferrite, which has a bcc (body centered cubic) structure. With decreasing temperature, δ -ferrite transforms to γ -austenite, fcc (face centered cubic) form of iron which can take up to 2.1 wt.% carbon.

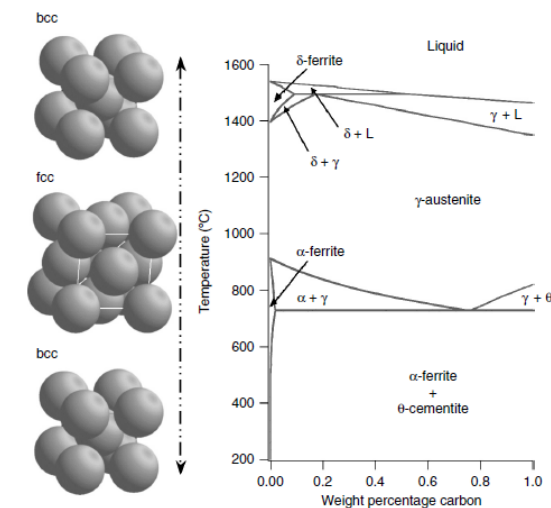


Fig.4: Fe-C phase diagram showing allotropic forms of Iron [1]

At lower temperatures, α -ferrite, another allotropic form of iron becomes stable, which has a bcc structure and can dissolve a small amount of carbon, up to a maximum of 0.02 wt% at 723°C. This large difference in carbon solubility of austenite and α -ferrite implies that steels are heat treatable. When cooling from austenitic temperature, austenite may decompose to different microstructures as ferrite, pearlite, bainite and martensite, making it possible to obtain a wide variety of mechanical properties by controlling the process variables. To have a better understanding of steels in general,

these microstructure evolutions need to be studied in detail. However, more focus is put on the martensitic and bainitic transformations due to their dominance in sinter-hardening process.

2.3.1 Ferritic and pearlitic transformations:

The product of the eutectoid transformation in steels is called pearlite, which is in fact a lamellar mixture of ferrite and cementite developed alternately during slow cooling of austenite. Considering the Fe-C phase diagram shown in Fig.4, the eutectoid transformation at 723°C may be written as;



Application of lever rule at this temperature gives the amount of cementite within the pearlite colonies;

$$\frac{0.77 - 0.02}{6.67 - 0.02} \times 100 = 11 \text{ wt\%}$$

and therefore, the weight percent of ferrite is 89%. This simple calculation shows that the pearlite basically contains 89% ferrite, and consequently similar thermal properties can be used for these phases in numerical modeling.

Pearlite and ferrite transformations are good examples of the diffusional process. The term diffusional implies that this transformation is controlled by diffusion process and is a function of both time and temperature. Thus, the kinetics of transformations can be simulated by application of the volume extended concept introduced by Johnson, Mehl, Avrami and Kolmogorov (see section 2.4.1).

2.3.2 Martensitic transformation:

Rapid cooling of steels from austenitic region may lead to formation of martensite. Unlike austenite to ferrite and pearlite transformations, formation of martensite is diffusionless. This implies that the elements in solid solution in the former austenite, remains in solution in the martensite. Therefore, martensite can be considered as a supersaturated solid solution of carbon in ferrite. This transformation is accompanied by a large shear deformation and a volume expansion, since the carbon atoms order within interstitial sites, in such a way that the bcc structure of ferrite changes to the body-centered tetragonal (bct) structure, shown in Fig.5a. The degree of tetragonality can be evaluated by measuring the ratio between the axes, c/a [6];

$$\frac{c}{a} = 1 + 0.045 \text{ wt\% C} \quad (2)$$

The effect of carbon content on lattice parameters, c and a , are shown in Fig.5b, showing that tetragonality increases dramatically with higher carbon dissolution.

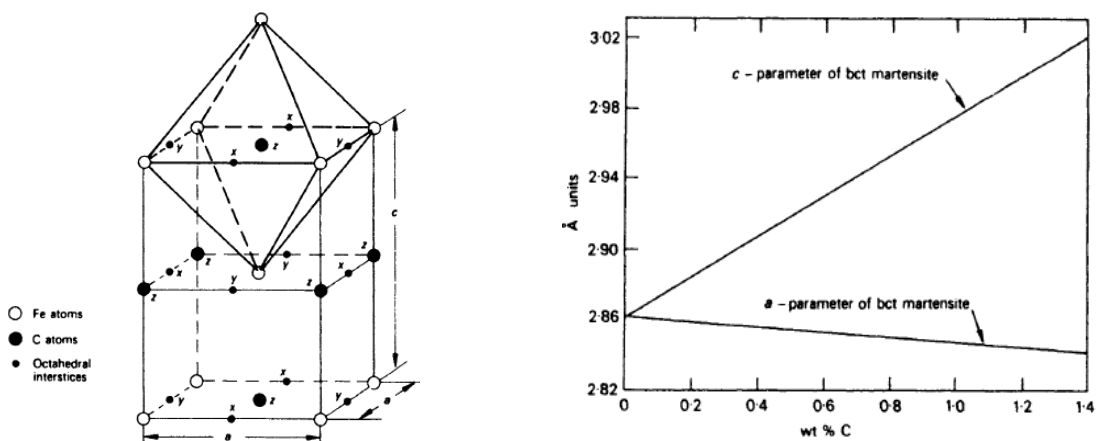


Fig.5 a) bct structure of martensite b) effect of carbon on lattice parameters, a and c [6]

Martensitic transformation is commonly considered as athermal, since the transformation starts at a well-defined temperature, M_s (i.e. martensite start temperature), and continues until martensite finish temperature, M_f , is reached. However, isothermal martensitic transformation may also occur at constant temperatures [6, 7].

2.3.2.1 Thermodynamics aspects of martensitic transformation in steels

Diffusionless nature of martensitic transformation implies that no chemical decomposition occurs during transformation; and therefore the chemical free energies of the martensite and the parent phase depend only on temperature. There may exist a specific temperature (T_0), at which these two free energies become equal. The difference between free chemical energy of austenite and martensite, at temperatures other than T_0 can be given as;

$$\Delta F^{\gamma \rightarrow \alpha} = F^\alpha - F^\gamma \quad (3)$$

Where, F^γ and F^α are chemical free energies of austenite and martensite, respectively. It has to be noted that, difference between chemical energies, $\Delta F^{\gamma \rightarrow \alpha}$, is positive when austenite is more stable than martensite. Fig.6 shows the variation of free energy with temperature for these phases. As can be seen, martensitic transformation does not take place until a certain supercooling is provided (M_s lies below T_0), due to the presence of nonchemical free energies such as interfacial and strain energies. In practice, the supercooling ($T_0 - M_s$) may exceed to a value as large as 200°C [8].

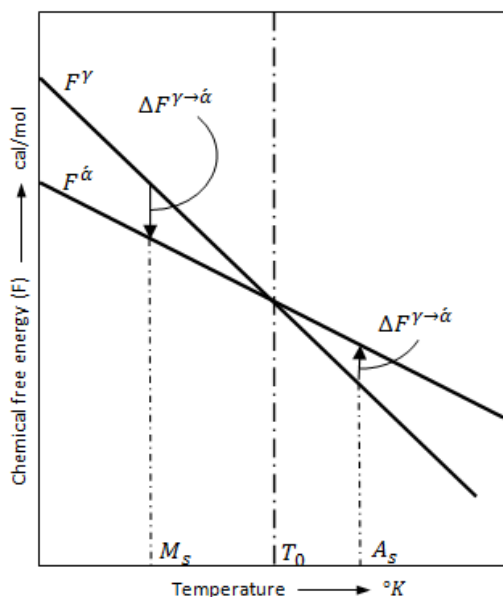


Fig.6: Variation of chemical free energy for austenite and martensite with temperature (after Kaufman and Cohen [8] with some modification)

One may express the overall free energy as;

$$\Delta W^{\gamma \rightarrow \alpha} = \Delta F^{\gamma \rightarrow \alpha} + \Delta G^{\gamma \rightarrow \alpha} \quad (4)$$

where, $\Delta G^{\gamma \rightarrow \alpha}$ represents the fraction of nonchemical free energies. The necessary condition for commence of martensitic transformation is that the overall free energy becomes negative, or $\Delta F^{\gamma \rightarrow \alpha} < \Delta G^{\alpha \rightarrow \gamma}$. In other words, not only is it necessary that the chemical free energy is negative, but it also needs to be less than a certain quantity, $\Delta G^{\alpha \rightarrow \gamma}$.

The classical theory of homogenous nucleation can be applied to study the martensitic transformation. In general, creation of new interfaces during solid state transformations will increase the free energy by an amount that depends on coherency of the parent phase (austenite) and the martensite. For a lenticular plate, with thickness of $2c$ and radius of $r \gg c$, the interfacial free energy may be given as;

$$\Delta G_s^{\gamma \rightarrow \alpha} = 2\pi r^2 \sigma \text{ cal/particle} \quad (5)$$

where, σ represents the free energy of α/γ interface per unit area, or specific interfacial free energy. Fisher et al. [9] assumed a coherent interface between the martensite and the parent phase, and calculated a value of $5.7 \times 10^{-7} \text{ cal/cm}^2$ for σ . On the other hand, it can be shown that if the interface between them is considered semi-coherent, higher values for the specific interfacial free energy can be obtained ($1.2 - 2.4 \times 10^{-5} \text{ cal/cm}^2$)[8].

Mechanical free energy is also an important factor, since the martensitic transformation is accompanied by large shear deformations. As a result, elastic strains are developed and stored, both inside and around the martensite plates. The elastic free energy of a lenticular martensite plate may be expressed as;

$$\Delta G_e^{\gamma \rightarrow \alpha} = \pi c r^2 (Ac/r) \text{ cal/particle} \quad (6)$$

where two terms $\pi c r^2$ and Ac/r refer to the approximated volume of martensite plate and the strain free energy of a unit volume of martensite, respectively, and A is the strain energy factor. Fisher et al. [9] showed that elastic free energy can take values as large as 480 to 1140 cal/cm^3 . Within and around martensite plates, some extent of plastic deformation can also take place, to relax the developed shear strains. However, the energy needed for such deformations to occur is considerably large, and therefore its effect is generally regarded negligible.

After inserting Eq.5 and Eq.6 into Eq.4; the overall free energy may take the form;

$$\Delta W^{\gamma \rightarrow \alpha} = \pi r^2 c \Delta f^{\gamma \rightarrow \alpha} + 2\pi r^2 \sigma + \pi c r^2 (Ac/r) \quad (7)$$

where, $\Delta f^{\gamma \rightarrow \alpha}$ is the chemical free energy change per unit volume. Differentiating Eq.7 with respect to r and c determines the value of critical nucleus size, and finally the free energy barrier can be given as [8, 9];

$$\Delta W^* = 8192 \pi \theta^2 \sigma^3 / (27 \Delta f^4) \text{ cal/particle} \quad (8)$$

where, θ is a strain factor that depends on the elastic constant of the parent phase and shear angle of martensite plate [9]. It should be mentioned that, although Eq.5 to Eq.8 give some indications regarding the effects of nonchemical energies on the transformation mechanism, the energy barrier calculated by Eq.8, is large by several orders of magnitude, leading to dramatic deviation from experimental observations. This confirms that martensite nucleation occurs on pre-existing embryos, and therefore, the whole mechanism is heterogeneous [6, 8].

2.3.2.2 Effects of alloying elements

The overall free energy of the martensitic transformation includes two separate terms, one is concerning the nonchemical free energies, discussed in previous section, and the other pertains to the chemical free energy, which will be studied here. In general, the alloying elements can influence both the chemical and nonchemical energies.

Since no chemical decomposition takes place during martensitic transformation, the chemical free energy of a binary $Fe - X$ alloy system can be expressed formally by adding three following terms;

$$\Delta F_{Fe-X}^{\gamma \rightarrow \alpha} = (1-x)\Delta F_{Fe}^{\gamma \rightarrow \alpha} + x\Delta F_X^{\gamma \rightarrow \alpha} + \Delta F_M^{\gamma \rightarrow \alpha} \quad (9)$$

where x is the concentration of alloying element X in atom fraction. In above relation, $\Delta F_M^{\gamma \rightarrow \alpha}$ represents the difference in the free energy of mixing. According to the basic rules of thermodynamics, $\Delta F_X^{\gamma \rightarrow \alpha}$ can be written as;

$$\Delta F_X^{\gamma \rightarrow \alpha} = \Delta H_X^{\gamma \rightarrow \alpha} - T\Delta S_X^{\gamma \rightarrow \alpha} \quad (10)$$

where $\Delta H_X^{\gamma \rightarrow \alpha}$ and $\Delta S_X^{\gamma \rightarrow \alpha}$ are the enthalpy and entropy changes between γ and α for the element X , respectively. Zener assumed that the solid solutions are ideal, which implies $\Delta F_M^{\gamma \rightarrow \alpha} = 0$ [8]. He further assumed that $\Delta S_X^{\gamma \rightarrow \alpha}$ is zero, and therefore Eq.9 can be simplified as;

$$\Delta F_{Fe-X}^{\gamma \rightarrow \alpha} = (1-x)\Delta F_{Fe}^{\gamma \rightarrow \alpha} + x\Delta H_X^{\gamma \rightarrow \alpha} \quad (11)$$

The values of $\Delta H_X^{\gamma \rightarrow \alpha}$ for different alloying system can be found in Ref.10. By setting $\Delta F_{Fe-X}^{\gamma \rightarrow \alpha}$ equal to zero, the value of T_0 can be obtained. In general, those elements that expand the γ loop, i.e. γ stabilizers, make the value of $\Delta H_X^{\gamma \rightarrow \alpha}$ positive and lower T_0 . Fig.7 shows the M_s and T_0 for iron-carbon and iron-nickel [8].

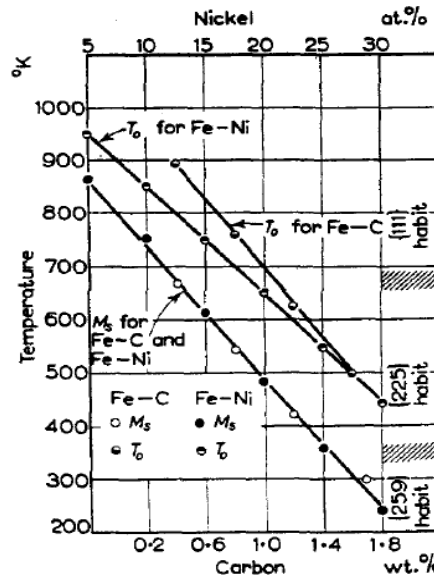


Fig.7: M_s and T_0 for iron-carbon and iron-nickel [8]

As can be seen, M_s and T_0 behave similarly, i.e. they both decrease as the alloying content increases. However, for the case of Fe-Ni, the difference between them, $T_0 - M_s$, increases with nickel content. This indicates that, the alloying elements may also take part in nonchemical free energies. Electron microscopy observations confirm that the martensitic transformation involves a large amount of slip or twining. Thus, anything that can restrain the glide of dislocations may retard the transformation temperature. Ghosh and Olson [11] suggested that the fraction of alloying elements in solid solution in austenite can be used to estimate the driving force necessary for martensitic transformation. Their hypothesis was based on the effects of solid solution strengthening mechanism on glide of dislocations. They showed that the critical driving force can be expressed in term of interfacial frictional work;

$$-\Delta G_{crit}^{\gamma \rightarrow \alpha} = K_1 + W_\mu(K_\mu^i, X_i) \quad (12)$$

where K_1 is a constant that includes the effects of interfacial energies and strain field around the embryo, and W_μ is the frictional work, given as;

$$W_\mu = \sqrt{\sum_i (K_\mu^i X_i^{0.5})^2} + \sqrt{\sum_j (K_\mu^j X_j^{0.5})^2} + \sqrt{\sum_k (K_\mu^k X_k^{0.5})^2} + K_\mu^{Co} X_{Co}^{0.5} \quad (13)$$

where $i = C, N ; j = Cr, Mn, Mo, Nb, Si, Ti, V; k = Al, Cu, Ni, W$. Using K_μ^i values reported in Ref.11; the critical driving force takes the form;

$$-\Delta G_{crit}^{\gamma \rightarrow \alpha} = K1 + 4009X_C^{0.5} + 1879X_{Si}^{0.5} + 1980X_{Mn}^{0.5} + 172X_{Ni}^{0.5} + 1418X_{Mo}^{0.5} + 1868X_{Cr}^{0.5} + 1618X_V^{0.5} + 752X_{Cu}^{0.5} + 714X_W^{0.5} + 1653X_{Nb}^{0.5} + 3097X_N^{0.5} - 352X_{Co}^{0.5} \quad (14)$$

Ghosh and Olson [11] reported a value of $K1 = 1010 J mol^{-1}$. Finally, it was assumed that the martensitic transformation commences when the chemical deriving force of austenite to martensite transformation reaches to $\Delta G_{crit}^{\gamma \rightarrow \alpha}$, that is;

$$\Delta F^{\gamma \rightarrow \alpha} \{at M_s\} = \Delta G_{crit}^{\gamma \rightarrow \alpha} \quad (15)$$

It should be noted that Cool and Bhadeshia [12] observed a better correlation between experimental data for $K1 = 683 J mol^{-1}$. There are also several empirical equations to calculate the martensite start temperatures. Andrews developed a product equation with confidence of $\pm 25^\circ C$ for 95% of the steels under investigation [7];

$$Ms(^{\circ}C) = 512 - 453C - 16.9Ni + 15Cr - 9.5Mo + 217(C)^2 - 71.5(C)(Mn) - 67.6(C)(Cr) \quad (16)$$

However, it was reported that for steels with high alloy content, the M_s calculated using such empirical equations (e.g. Eq.16) deviates dramatically from experimental values [13].

2.3.2.3 Effect of grain size

Several studies [14-17] reported the dependence of martensite start temperature on austenite grain size (AGS). As shown in Fig.8, the M_s drops as the AGS decreases, however, the influence of AGS is more significant for smaller grains. Many qualitative explanations for this observation have been given. For instance, Brofman and Ansell [14] proposed that this behavior can be explained by means of dislocation theories. Using the experimental evidence that confirms the inverse relation between grain size and dislocation density ($\rho \propto 1/D$) [18], they suggested that higher dislocation density within the smaller grains may have some strengthening effects on the austenite, leading to higher resistance to plastic deformations locally and macroscopically. Consequently, higher driving force is needed for martensitic transformation. Although this hypothesis gives an explanation for such behavior, there are some arguments against its viability [19]. Recently, Yang and Behadesha developed a model to estimate the variation of martensite start temperature as a function of the AGS. This model is, in fact, based on the geometrical partitioning hypothesis introduced by Fisher et al. (9), which suggests that the amount of the transformed martensite, during the early stages of transformation, is proportional to cube of austenite grain size ($V_f \propto D^3$). Thus, for smaller grains, higher undercooling is needed to detect the early stages of martensitic transformation corresponding to M_s . Although the model proposed by Yang and Behadesha is shown viable, the need for the reliable thermodynamic databases restricts its application. Lee and Lee [20] proposed an empirical equation for low alloy steels that considers the effects of chemical composition and austenite grain size on martensite start temperature;

$$Ms(^{\circ}C) = 402 - 797C + 14.4Mn + 15.3Si - 31.1Ni + 345.6Cr + 434.6Mo + (59.6C + 3.8Ni - 41Cr - 53.8Mo).G \quad (17)$$

where G is the ASTM austenite grain size and elements are in weight fraction.

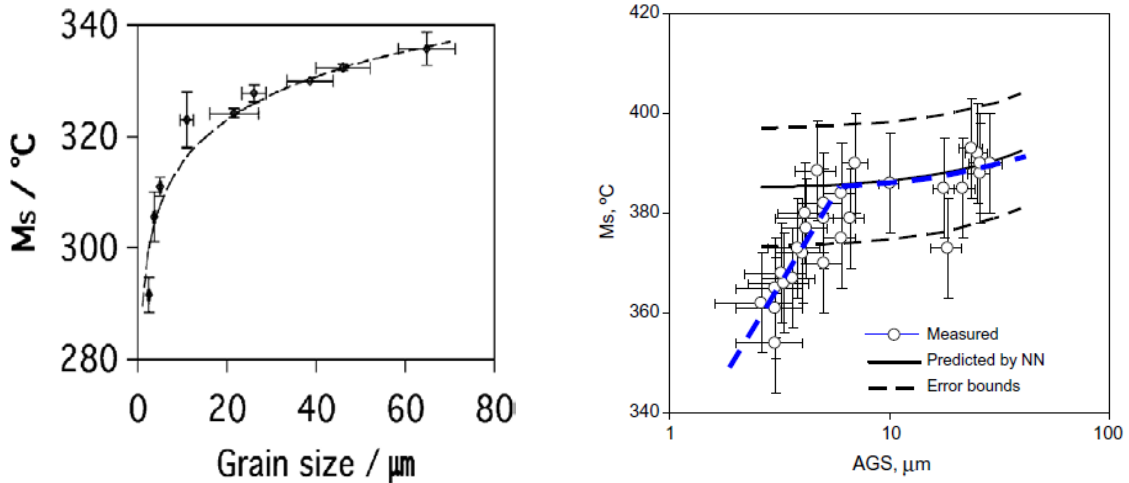


Fig.8: variation of martensite start temperature against grain size [17, 19]

2.3.2.4 Surface effects on martensite start temperature

In general, the lattice energy is higher at the surface of the crystals, leading to a smaller barrier for nucleation [10]. However, the energy difference between the surface and interior of a crystal depends on the chemical composition and the crystal orientation. In particular, for the case of martensitic transformation, the effect of free surfaces can be described by its influence on relative stability of structure at the surface [21]. The shear nature of the martensitic transformation suggests that any phenomenon that can ease the glide on dislocations will promote the transformation, and consequently, affects the martensite start temperature. In this sense, the energy barrier for martensitic transformation is smaller at the surface, since restraining effects of the neighboring atoms on shear deformation is partly eliminated at the surface. Several studies have been conducted to experimentally confirm the promoting effects of free surfaces on martensitic transformation. For instance, Honma [10] measured the M_s at the surface and in the interior for several $Fe - Ni$ alloys, and showed that martensite start temperature is higher by 10-30 °C at the surface layer. Further details on experimental investigations and verifications can be found in Ref.10.

2.3.2.5 Kinetics of martensitic transformation in steels

Several equations have been developed to describe the kinetics of athermal martensitic transformation. However, the reliability of these equations is still under investigation. Fig.9 shows the comparison between the models proposed by different authors. As can be seen, all three models agree closely for undercooling less than 50 °C, but they diverge markedly for higher undercoolings. The discrepancy between the predicted volume fractions is probably due to the different methods they used to measure the amount retained austenite. The model proposed by Koistinen and Marburger [22] is known the most viable relation (referred to as KM model), since X-ray analysis was used to determine the volume fraction of retained austenite. They showed that the extent of martensitic transformation for pure iron-carbon alloys can be expressed as;

$$V = 1 - \exp(-0.011(M_s - T)) \quad (18)$$

where V is the volume fraction of martensite transformed and T is the temperature below M_s .

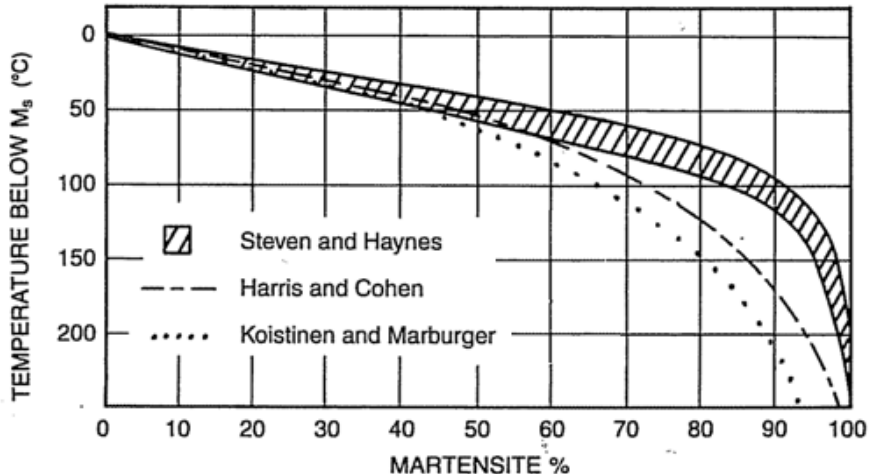


Fig.9: Martensite formation as a function of undercooling below Ms [7]

Several authors have used this equation to predict the extent of martensitic transformation for low alloy steels. However, recent study conducted by Lee-Lee [20] shows that this model cannot completely predict the extent of transformation for low alloy steels. They, therefore, made an attempt to develop a new model using dilatometric analysis of a wide range of low alloy steels [20];

$$\frac{dV}{dT} = K \cdot V^a (1 - V)^b \quad (19)$$

$$K = \frac{G^{0.240} (M_s - T)^{0.191}}{9.017 + 62.88C + 9.27Ni - 1.08Cr + 0.76Mo}$$

$$a = 0.42 - 0.246C + 0.359C^2$$

$$b = 0.32 - 0.567C + 0.933C^2$$

where V is the volume fraction of martensite and C is the carbon content in wt% and G is the ASTM austenite grain size.

2.3.3 Bainitic transformation:

Bainite is an intermediate product, in the sense that it forms at temperatures above martensite start temperature but below those at which the pearlitic transformation can take place. Bainite is a mixture of carbide and ferrite; however, microscopically, it is quite different from pearlite. The major difference is that, unlike pearlite, the cementite and ferrite in bainite possess a certain orientational relation with the parent phase within the grains [24]. There are mainly two forms of bainite, upper and lower bainite.

Upper bainite forms at temperature range 550 °C -400 °C. The main microstructural feature of upper bainite is its feathery appearance of the ferrite clusters, often called sheaves [6, 7]. Within each sheaf the plates of ferrite (sub-units) are parallel, having similar crystallographic orientation [6]. Decomposition of austenite to upper bainite takes place in two distinct stages. Firstly, the ferrite plates nucleate at the austenite grain boundaries, and then they grow rapidly within the grains. This process is accompanied by large shear deformations, thus in one sense, the bainitic transformation is similar to low temperature martensitic transformation [6]. However, upper bainite forms at higher temperatures at which the strength of austenite is significantly lower. Therefore, some amount of the shear strain developed during rapid growth of ferrite plates can be relaxed by plastic deformation of the nearby high temperature austenite. This plastic deformation is accompanied by an increase in dislocation density, which in turn strengthens the adjacent austenite. Due to this strengthening effect, the sub-units can grow to a limited size which is much smaller than the austenite grain size. Since the solubility of carbon in ferrite is 0.02 wt% at most, during the growth of plates, the carbon

solute transfers into adjacent austenite. Eventually, the carbon concentration reaches to the critical value necessary for carbide precipitation, and cementite forms between the ferrite sub-units. Lower bainite, in contrast, forms at lower temperature range 400-250°C. Crystallographic and microstructural features of the lower bainite are very close to the upper bainite; however, the mechanism of carbide precipitation is slightly different. In lower bainite, the carbides may also form inside the ferrite plates as a result of supersaturation. However, these cementite particles are very fine and cannot be resolved by optical microscopy.

2.3.3.1 Kinetics of bainitic transformation

Bhadeshia [23] suggests that the bainitic transformation may take place in two distinct stages, shown in Fig.10. Firstly, it starts with nucleation of a sub-unit at an austenite grain boundary, which grows rapidly within the grains before it is suppressed by the plastic deformation of adjacent austenite. Then, new sub-unit may nucleate at the tip and the ferrite clusters form. As this process continues, the carbide may also precipitate within the supersaturated ferrite plates, or the enriched nearby austenite. The overall kinetic of bainite evolution is controlled by these three events, and may be expressed by the concept proposed by Johnson, Mehl, Avrami and Kolmogorov [23].

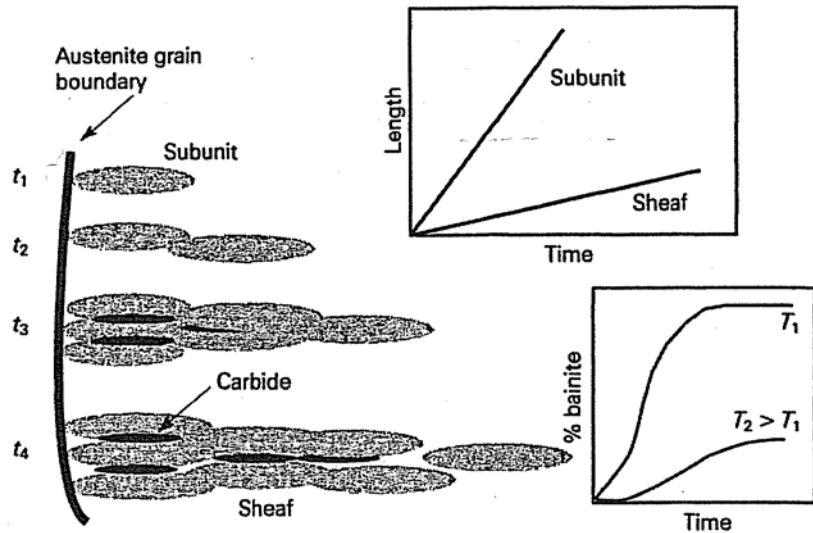


Fig.10: evolution stages of bainitic transformation [6]

2.3.3.2 Effect of austenite grain size

The effect of austenite grain size on kinetics of bainite transformation is not well understood. Some studies showed an inverse relation between grain size and transformation rate, while others reported that the overall kinetics of bainite reaction increases with increasing the grain size [23]. A detailed study conducted by Bhadeshia [23] suggests that there is a relation between the bainite morphology and the grain size effects, which may explain the discrepancy in experimental observations for different steels. Fig.11 shows the morphology of bainite for two different low alloy steels, at early stages of transformation [25]. Two extreme cases may occur;

1. The nucleation rate at the grain boundaries is relatively lower than the growth rates of the bainite sheaves (steel A)
2. The nucleation rate at grain boundary is higher than growth rates of the bainite sheaves (Steel B)

In steel A, bainite sheaves lengthened within the grains until their growth was stopped by grain boundaries. In this case, the maximum volume of a sheaf is directly proportional to the cube of austenite grain size, $V_{max} \propto D^3$. Thus, for steel A, the overall kinetics of transformation is suppressed

by reducing the grain size. On the other hand, for the case of Steel B, the nucleation rate is relatively higher than growth rate of bainite sheaves and the number of nucleation sites specifies the overall reaction rate. Thus, with decreasing the austenite grain size, the number of potential sites for nucleation increases, and consequently the overall reaction rate increases with reducing the grain size.

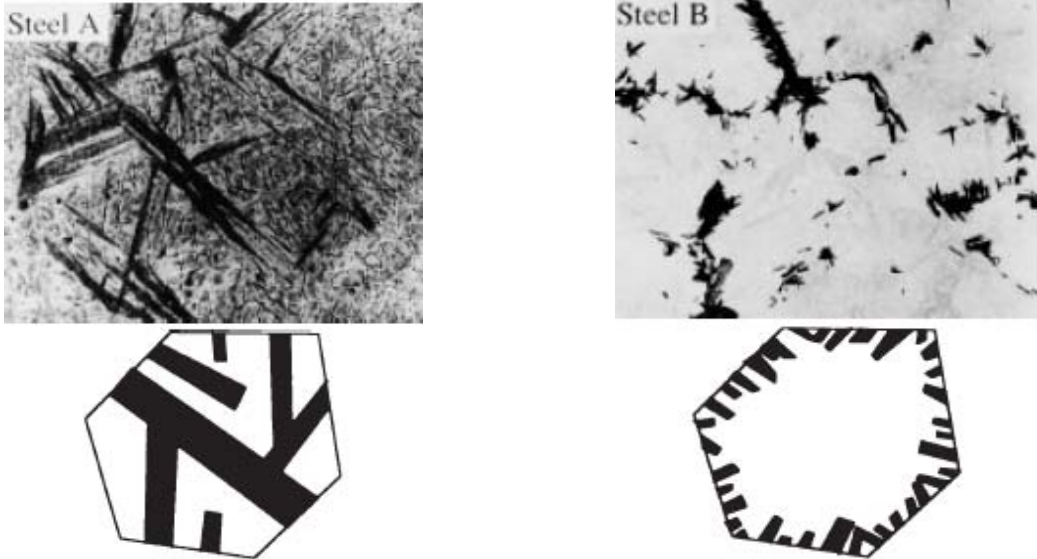


Fig.11: bainite morphologies for two different steels [25]

2.4 Kinetic models for diffusive transformations

Phase transformation in steels is generally divided into two groups, diffusional and diffusionless transformations. As discussed before, the diffusive transformation involves nucleation and growth mechanisms that are both time and temperature dependent, while the extent of the diffusionless transformation is solely a function of undercooling. Several models have been proposed to describe the kinetics of diffusion controlled, as well as, diffusionless or martensitic transformations in steels.

2.4.1 Johnson–Mehl–Avrami–Kolmogorov (JMAK) model

Johnson, Mehl, Avrami and Kolmogorov developed a model to determine the extent of the diffusive transformations under isothermal conditions [26]. Their model is based on the following assumptions [6, 26];

1. The nucleation process is random
2. The nucleation and growth rates are constant with respect to time
3. The nuclei have spherical shape

Under these assumptions, they showed that the volume fraction of the transformed phase X , at any given time t , can be obtained by;

$$X = 1 - \exp\left(-\frac{\pi}{3} \dot{N} G^3 t^4\right) \quad (20)$$

where \dot{N} is the nucleation rates and G is the growth rate of the spherical nuclei. However, in actual practice, this simple model cannot cover all the possibilities during nucleation and growth process. For instance, grain boundaries act as the preferential sites for nucleation process and can enhance the rate of nucleation markedly. Therefore, one may express the JMAK model in a general form;

$$X = 1 - \exp(-k(T)t^{n(T)}) \quad (21)$$

where k and n are the model's parameters and depend on the nucleation and growth mechanism. When the isothermal transformation diagram is available, these parameters can be obtained by means of the following relations;

$$n = \frac{\ln(\ln(1-X_s)/\ln(1-X_f))}{\ln(t_s/t_f)} \quad (22)$$

$$b = -\frac{\ln(1-X_s)}{t_s^n} \quad (23)$$

where X_s and X_f are the starting and finishing volume fractions, usually taken as $X_s = 0.01$ and $X_f = 0.99$ and, t_s and t_f are respectively the start and finish transformation times at a constant temperature. Time derivative of Eq.21 takes the form of the following equation;

$$\dot{X} = b^{1/n}(n(1-X)(-\ln(1-X))^{n-1/n}) \quad (24)$$

If n in Eq.21 remains constant during transformation (i.e. n stays independent of temperature), and k is only a function of temperature, the rate equation Eq.24, can be expressed as $f(X)g(T)$, and the transformation is called iso-kinetic. It will be discussed later that, in such circumstances, *Scheil's principle* can be used to extend the JMAK model for anisothermal condition.

It takes an enormous effort to produce a TTT diagram. Generally, for a given steels composition, only one TTT diagram is available, which is provided for a specific austenite grain size and austenitizing temperature. In order to consider the difference between the austenite grain sizes reported in TTT diagrams ($d\gamma_{TTT}$) and its size within the samples ($d\gamma$), one may use the modified JMAK model [27] ;

$$X = 1 - \exp(-k(T)(\frac{d\gamma_{TTT}}{d\gamma})^q t^n) \quad (25)$$

where q is to be taken 1 for ferrite and 2 for pearlite transformations.

2.4.2 Austin and Rickett (AR) model

Several authors [28, 29] used the Austin-Rickett (AR) equation to describe the kinetics of diffusional transformations with time;

$$\log\left(\frac{X}{1-X}\right) = m\log(t) + c \quad (26)$$

where m and c are the model's parameters, which can be obtained using TTT digarams. Starink [30] showed that this model can predict the kinetics of diffusion controlled transformations more precisely than the JMAK model. The rate of transformation can be obtained by differentiating Eq.26 with respect to time;

$$\frac{dx}{dt} = m10^{c/m} X^{\left(1-\frac{1}{m}\right)} (1-X)^{\left(1+\frac{1}{m}\right)} \quad (27)$$

The volume fraction of the transformed phase can be calculated by integration of Eq.27 with respect to time. However, the initial value $X = 0$ at the beginning of the transformation results in zero transformation rates. Tehler [29] suggested the following modification to tackle this problem;

$$X = \begin{cases} X & X > 0.0001 \\ 0.0001 & X < 0.0001 \end{cases}$$

2.4.3 Kirkaldy equations

Kirkaldy and Venugopalan [31] proposed a series of rate equations for diffusive transformations in steels, in a general form of,

$$\frac{dX}{dt} = \frac{(\Delta T)^n \exp\left(-\frac{Q}{RT}\right)}{F(C, Mn, Si, Ni, Cr, Mo, G)} X^{\frac{2(1-X)}{3}} (1-X)^{\frac{2X}{3}} \quad (28)$$

where F is a function of alloying elements in wt%, G is the prior austenite grain size (ASTM number), ΔT is the undercooling, and Q is the activation energy of the diffusional reaction. The exponent of undercooling n is a constant concerning the diffusion mechanism ($n = 2$ for volume diffusion in case of bainitic transformation and $n = 3$ for boundary diffusion in case of ferrite/pearlite transformations). Application of Scheil's additivity rule (see section 2.4.4) together with time integration of Eq.28 over time-temperature profile gives the volume fraction of transformed phase under any arbitrary cooling condition; ,

$$X = \int_0^X dX = \int_0^t \frac{dX}{dt} dt = \int_0^t \frac{(\Delta T)^n \exp\left(-\frac{Q}{RT}\right)}{F(C, Mn, Si, Ni, Cr, Mo, G)} X^{\frac{2(1-X)}{3}} (1-X)^{\frac{2X}{3}} dt \quad (29)$$

In general, the function F , the exponent n and the activation energy vary for ferrite, bainite and pearlite transformations. ΔT is the difference between the equilibrium temperatures, A_1 , A_3 and B_s , and the instantaneous temperature during cooling.

2.4.4 Scheil's principle

The models defined in sections 2.4.1 to 2.4.3 give a mathematical description of the transformation kinetics under isothermal condition. In common heat treating processes, except for some special cases in thermomechanical treatments, anisothermal condition (also referred to continuous cooling condition) is more frequent. However, in such circumstances, the aforementioned models are of no practical use. To tackle this limitation, Scheil proposed a hypothesis to calculate the incubation time under anisothermal condition from isothermal data, which is widely known as *Scheil's principle* or *Scheil additivity rule* [32]. According to this hypothesis, the time needed to reach a specific amount of transformed phase, X , under anisothermal conditions can be obtained, when the following relation is satisfied;

$$\int_0^t \frac{d\xi}{\tilde{\tau}(T(\xi), X(t))} = 1 \quad (30)$$

where $\tilde{\tau}(T, X)$ is the time needed to reach the same fraction of X in isothermal condition. The incubation time of the transformation can be calculated applying similar hypothesis;

$$\int_0^t \frac{d\xi}{\tau_s(T(\xi))} = 1 \quad (31)$$

where $\tau_s(T)$ is the isothermal incubation time corresponding to $X = 1\%$ at a given temperature, which is simply available in TTT diagrams. Fig.12 shows the schematic representation of the Scheil additivity rule.

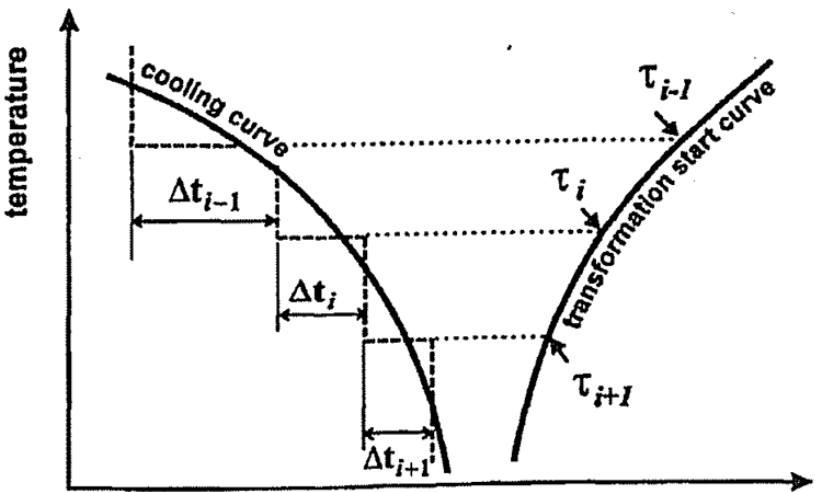


Fig.12: schematic representation of the Scheil additivity rule [32]

It is shown that this additivity hypothesis is valid only if transformation is iso-kinetic. In this circumstance, the rate equation can be written as a separate function of X and T [33] ;

$$\dot{X} = f(X)g(T) \quad (32)$$

Referring back to Eq.24 and Eq.27, the necessary condition for JMAK and AR models to be written in the form of Eq.32 is that the exponents n and m are to be constant and b and c are only functions of temperature. However, in practice, this condition is rarely satisfied during phase transformation process. For instance, the values of n in JMAK model obtained from Eq.22 vary markedly with temperature, and can hardly be considered as a constant.

Hawbolt and his co-workers [34] experimentally confirmed that the additivity rule does not hold for incubation period and when n varies markedly with temperature the application of the additivity rule leads to overestimation in calculation of the time needed for completion of pearlitic transformation. However, they found that if the incubation period is excluded from the whole transformation period, the exponent n is virtually constant, leading to an iso-kinetic transformation. It is worthy to note that in order to determine the parameters of the JMAK model; several researchers [32] have directly used Eq.22 and Eq.23 without taking into account the fraction of error introduced by inclusion of incubation period. However, recent study conducted by Zhu et al. [35] showed that the fraction of error due to the inclusion of incubation time in calculations is small, despite the fact that according to Hawbolt et al. [34] the additivity rule does not hold for incubation period.

2.4.5 Effects of porosity on the kinetics of transformations

Porosity may affect the kinetics of transformation by several means. It is known that the most effective potential sites for nucleation of the diffusive products are the free surfaces and grain boundaries [24]. The porous nature of PM steels implies that this type of materials possess a larger amount of potential sites for nucleation process (due to the presence of free surfaces) compared to the conventional solid steels. Pores may also inhibit the grain growth at elevated temperatures due to the pinning effects [36, 37], leading to relatively smaller grain sizes than it can be found in fully dense steels with similar chemical composition, heat treated under the same condition. Warke et al. [38, 39] have conducted a detailed study on kinetics of diffusional transformation of a prealloyed PM steel. They found that the presence of porosity in PM steels decreases the austenite stability, and therefore, the incubation time reduces with increasing porosity content. The metallographic and dilatometric results provided in Ref.39 confirm that the presence of porosity can promote both the nucleation and growth mechanisms by increasing the amount of potential sites and the effective diffusion path in porous steels. Several authors reported a similar trend [40-42].

In general, several factors may affect the kinetics of athermal (martensitic) transformation in steels. Different aspects of martensitic transformation were discussed in section 2.3.2. It is shown that M_s is highly sensitive to variation of interstitial alloying elements such as carbon and nitrogen. It is also shown that M_s reduces with decreasing the grain size, while the free surfaces can reduce the energy barrier for martensitic transformation, leading to an increase in M_s . Hence, the porous nature of PM steels may affect the martensite start temperature by several means, in particular, the larger amount of free surfaces and likelihood of carbon fluctuation close to the pores may increase the M_s by several degrees compared to the wrought steels with similar chemical compositions. On the other hand, smaller austenite grain size in PM steels may lead to a decrease in martensite start temperature. However, as can be seen in Fig.8, the effect of austenite grain size on martensite start temperature is significant for grains smaller than $10 \mu\text{m}$, which is not usually the case in PM steels, and therefore can be neglected.

Several authors [39, 40] reported the same trend in dependence of M_s to the level of porosity. In a very recent study, Warke et al. [39] experimentally confirmed that the martensite start temperature in PM steels increases with increasing the porosity content. Based on these experimental results, Semel and Lados [43] suggested that the M_s in PM steels increases by 2.3°C per 1% porosity.

2.5 Constitutive equation and finite element formulation

In order to study the cooling behavior of a material under a specific condition, it is necessary to solve the heat equation. However, except for some simple cases, solving the heat equation requires complicated mathematical treatments, and often application of numerical methods such as Finite Difference Methods (FDM) and Finite Element Methods (FEM) is inevitable.

In this part, an attempt is made to provide a brief description of the general form of heat equation, including the latent heats of solid phase transformation. Then, the FE formulation of the axisymmetric heat equation has been developed, and finally the procedure to couple the phase transformation terms has been described.

2.5.1 Constitutive equation

Heat equation, in its general form, can describe the temperature distribution within any arbitrary region over the time. It can be derived using Fourier's law of heat conduction and the law of conservation of energy as [44];

$$\rho \frac{\partial E}{\partial t} - \nabla(k\nabla T) = 0 \quad (33)$$

where ρ , k , T and t are density, thermal conductivity, temperature and time, respectively. E is the specific internal energy. There may exist a differentiable function e , representing the specific internal energy within the material as;

$$E(x, t) = e(T, X_i) \quad (34)$$

where $X_{i=1,2,3,4}$ correspond to volume fractions of ferrite, pearlite, bainite and martensite phases, respectively. Differentiating Eq.34 with respect to the internal variables gives;

$$\frac{\partial e}{\partial T} = c \quad \text{and} \quad \frac{\partial e}{\partial X_i} = -q_i$$

where c is the specific heat and q_i represents the latent heats of i^{th} solid transformation. Thus, the general form of heat equation in two dimensional Cartesian coordinate system may be written as;

$$\rho(T)c(T)\frac{\partial T}{\partial t} = \frac{\partial}{\partial x}\left(k(T)\frac{\partial T}{\partial x}\right) + \frac{\partial}{\partial y}\left(k(T)\frac{\partial T}{\partial y}\right) + \sum \rho_i(T)q_i(T)\frac{\partial X_i}{\partial t} \quad \text{in region } \Omega \quad (35)$$

As shown in Eq.35, in general, all the thermal properties can be temperature dependent. The boundary and initial conditions may be given as;

$$-k \frac{\partial T}{\partial n} = h_c(T)(T - T_\infty) + \sigma\epsilon(T)(T^4 - T_\infty^4) \quad \text{along } \Gamma \text{ for air cooling} \quad (36)$$

$$-k \frac{\partial T}{\partial n} = h_c(T)(T - T_\infty) \quad \text{along } \Gamma \text{ for water/oil quenching} \quad (37)$$

$$T_0 = T(x, y, 0) \quad \text{at } t = 0 \text{ in region } \Omega \quad (38)$$

where h_c is the convective heat transfer coefficient, σ is the Stefan–Boltzmann constant (56.7 W/mm.K), ϵ is the radiation emissivity of the surface and T_∞ is the ambient temperature. Both h_c and ϵ can be a function of temperature. The radiative part of Eq.36 can be written as;

$$\sigma\epsilon(T)(T^4 - T_\infty^4) = \sigma\epsilon(T)(T^2 + T_\infty^2)(T + T_\infty)(T - T_\infty) = h_r(T)(T - T_\infty) \quad (39)$$

Therefore, Eq.36 may be expressed as;

$$-k \frac{\partial T}{\partial n} = h_c(T)(T - T_\infty) + h_r(T)(T - T_\infty) = h_{rc}(T)(T - T_\infty) \quad (40)$$

where, h_{rc} is often called the combined heat transfer coefficient, including both the radiative and convective parts. Eq.36 in cylindrical coordinate system takes the following form;

$$\rho(T)c(T) \frac{\partial T}{\partial t} = k(T) \left(\frac{1}{r} \frac{\partial}{\partial r} \left(r \frac{\partial T}{\partial r} \right) + \frac{\partial^2 T}{\partial z^2} \right) + \sum \rho_i(T) q_i(T) \frac{\partial X_i}{\partial t} \quad (41)$$

It is worthy to note that Eq.35 and Eq.41 are both based on an assumption that the temperature gradient in the third direction is negligible. nonetheless, these equations have many practical uses. As an example, the temperature distribution of the cylindrical geometries such as rings can be estimated with a reasonable precision using Eq.41. Fig.13 shows 3D geometry which can be simplified to a 2D axi-symmetric domain, provided that the boundray conditions are also axi-symmetric.

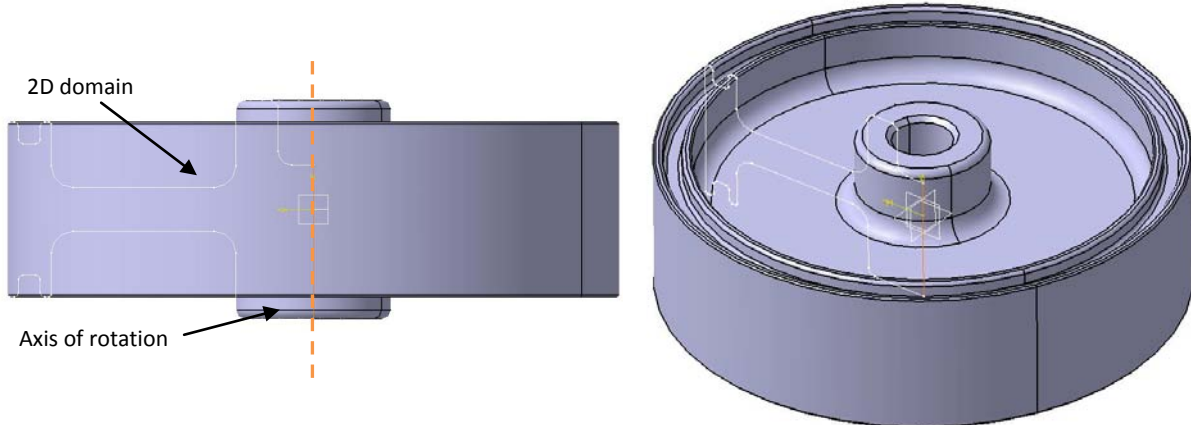


Fig.13: an illustrative 3D model which can be treated as a 2D domain according to axi-symmetric FE formulation

2.5.2 FE Formulation

In general, Eq.41 (or Eq.35) cannot be solved analytically, and therefore, application of numerical methods to obtain the temperature distribution is inevitable. FEM is a powerful numerical tool for solving Partial Differential Equations (PDE) such as Eq. 41, within any arbitrary domain with nonlinear

boundary and initial conditions. In this part, only a brief description of the FE formulation is provided, and an interested reader is referred to Ref.45 for more detailed treatments.

The weak form of Eq.41 is derived by multiplying it by an arbitrary weight function, ω , and using divergence theorem to incorporate the boundary conditions;

$$\int_{\Omega} \omega \rho c \frac{\partial T}{\partial t} r dr dz + \int_{\Omega} k \left(\frac{\partial \omega}{\partial r} \frac{\partial T}{\partial r} + \frac{\partial \omega}{\partial z} \frac{\partial T}{\partial z} \right) r dr dz + \int_{\Gamma} \omega r h_{rc} (T - T_{\infty}) d\Gamma - \int_{\Omega} \omega \sum \rho_i q_i \frac{\partial X_i}{\partial t} r dr dz = 0 \quad (42)$$

Application of the standard procedure of FE discretization, Eq.42 takes the general form of;

$$C \dot{T} + KT = R \quad (43)$$

where C is the heat capacity matrix, R is the vector of thermal loads and K represents the stiffness matrix. In order to obtain the temperature at new times, the so-called θ -method scheme can be used [45];

$$\dot{T} = \frac{T^{j+1} - T^j}{\Delta t} \quad (44)$$

where $T^j = T(r, z, t_n)$ is the temperature at time step j corresponding to time $t = t_j$, and Δt is the time increment. Thus, having known the temperature at current time, it is possible to calculate the temperature in the next time step. By introducing the relaxation parameter $0 < \theta < 1$, the absolute temperature can be obtained as;

$$T = \theta T^{j+1} + (1 - \theta) T^j \quad (45)$$

It is worthy to note that for $\theta \geq \frac{1}{2}$, the numerical algorithm is unconditionally stable. In this work, $\theta = \frac{2}{3}$ is assumed. Inserting Eq.45 and Eq.44 into Eq.43, we have;

$$\left(\theta K + \frac{1}{\Delta t} C \right) T^{j+1} = \left((\theta - 1) K + \frac{1}{\Delta t} C \right) T^j + R \quad (46)$$

K , C and R , in general, can be a function of temperature. This means that Eq.46 cannot be solved using direct FE methods. Thus, it needs to be written in a form of force-balance vector;

$$g(T^{j+1}) = \left(\theta K^{j+1} + \frac{1}{\Delta t} C^{j+1} \right) T^{j+1} - \left((\theta - 1) K^{j+1} + \frac{1}{\Delta t} C^{j+1} \right) T^j - R^{j+1} = 0 \quad (47)$$

where K^{j+1} , C^{j+1} and R^{j+1} are stiffness matrix, heat capacity matrix and load vector at temperature T^{j+1} . In time step j , T^j is known and T^{j+1} is sought. There are several numerical methods to find the roots of Eq.47. Newton iteration scheme is one of the most powerful methods to solve the nonlinear system of equations [45] that can be expressed as;

$$\begin{cases} J_m^{j+1} \Delta T_{m+1}^{j+1} = -g_m^{j+1} \\ T_{m+1}^{j+1} = T_m^{j+1} + \Delta T_{m+1}^{j+1} \end{cases} \quad (48)$$

where m is the iteration number in j^{th} time step, and J is the Jacobian matrix (or derivative matrix) at T^{j+1} ,

$$J(T^{j+1}) = \left(\theta K^{j+1} + \frac{1}{\Delta t} C^{j+1} \right) + \left(\theta \frac{\partial K^{j+1}}{\partial T^{j+1}} + \frac{1}{\Delta t} \frac{\partial C^{j+1}}{\partial T^{j+1}} \right) T^{j+1} - \left((\theta - 1) \frac{\partial K^{j+1}}{\partial T^j} + \frac{1}{\Delta t} \frac{\partial C^{j+1}}{\partial T^j} \right) T^j - \frac{\partial R^{j+1}}{\partial T^{j+1}} \quad (49)$$

In each time increment, a virtual temperature (T), starting from T^j , is updated using the scheme given in Eq.48, until the force balance vector lies below an error limit, consequently;

If $\|g(T)\| < \varepsilon$ then $T^{j+1} = T$

In this work, four-node isoparametric element is used. Using isoparametric formulations, the four-node plane element can be applied to any arbitrary domain. This concept is based on mapping the four-node element with non-parallel sides (with the global coordinate system) to a new coordinate system in such a way that the sides of the rectangular element become parallel to the coordinate axes in new system, as shown in Fig. 14. This ensures that the compatibility criterion for the element is met. Interested reader is referred to Ref.45 for more details on this type of elements.

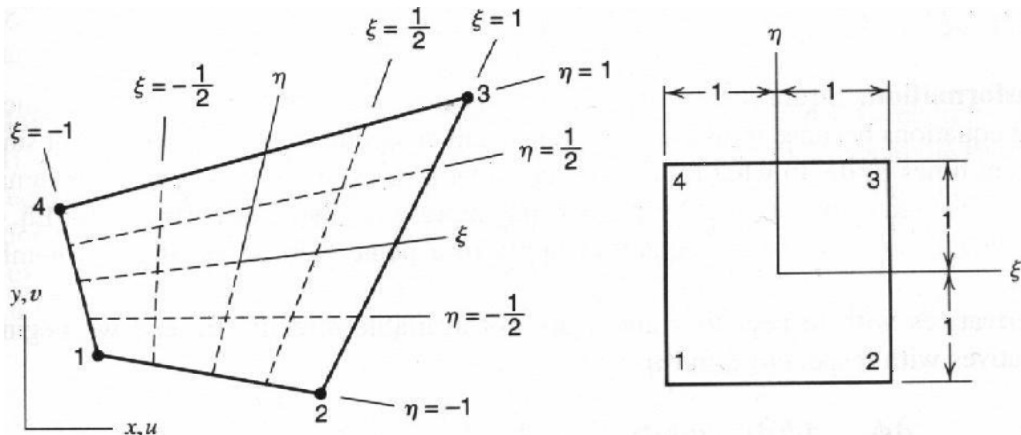


Fig.14: Isoparametric mapping of a four node plane element in global coordinate system (Left) to the $\xi\eta$ space (right) [45]

2.5.3 Incorporating the phase transformation terms

This section deals with incorporating the phase transformation models into the weak formulation, Eq.42. As pointed out earlier, the thermal load vector (R) in Eq.43 includes the terms concerning both the boundary conditions and the latent heat of phase change;

$$R = \int_{\Gamma} \omega r h_{rc} T_{\infty} d\Gamma + \int_{\Omega} \omega \sum \rho_i q_i \frac{\partial X_i}{\partial t} r dr dz \quad (50)$$

At constant pressures, the latent heats of transformation may be replaced by the enthalpy changes ($\rho q \equiv \Delta H$);

$$R = \int_{\Gamma} \omega r h_{rc} T_{\infty} d\Gamma + \int_{\Omega} \omega \sum \Delta H_i \frac{\partial X_i}{\partial t} r dr dz \quad (51)$$

As before, $i = 1,2,3,4$ represents ferrite, pearlite, bainite and martensite phases, respectively. Thus, for instance, ΔH_1 denotes the enthalpy change of austenite to ferrite transformation. When the time increments are infinitesimally small, one may make the following assumption;

$$R = \int_{\Gamma} \omega r h_{rc} T_{\infty} d\Gamma + \int_{\Omega} \omega \sum \Delta H_i \frac{\Delta X_i}{\Delta t} r dr dz \quad (52)$$

in which, it is assumed that;

$$\frac{\partial X_i}{\partial t} \cong \frac{\Delta X_i}{\Delta t} = \frac{X_i^{j+1} - X_i^j}{\Delta t} \quad (53)$$

In Eq.53, X_i^{j+1} represent the volume fraction of phase i at time step $j + 1$. It is also necessary to update the thermal properties during the phase transformation process. Having known the amount of each phase in time step j , the thermal properties can be calculated using the rule of mixture;

$$\rho c = \sum_{i=1,2,3,4,\gamma} X_i \rho_i c_i$$

$$k = \sum_{i=1,2,3,4,\gamma} X_i k_i$$

Both JMAK and AR models can be used to predict the amount of diffusive transformations, however in following paragraphs; the focus is put on implementation of the JMAK model.

According to Scheil' principle (see section 2.4.4), the kinetics of transformation under anisothermal condition can be approximated by means of infinitesimally small isothermal increments. Fig.15 shows the incremental time approach.

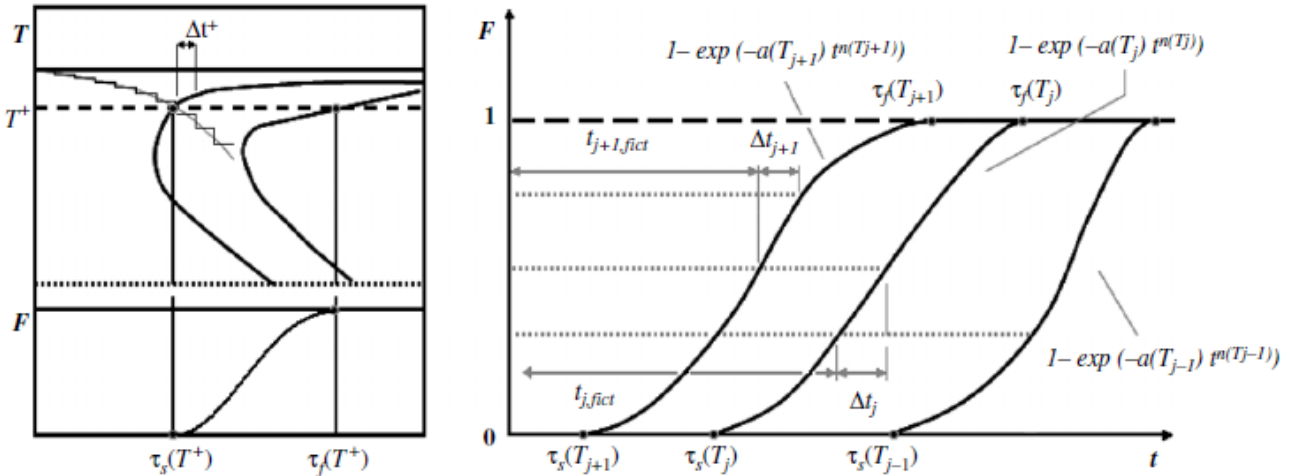


Fig.15: additivity rule, fictitious time [46]

Assuming that the volume fraction of phase i at the temperature T_{j-1} is known, the transformation time can be obtained by summation of the time increment, Δt , and a fictitious time, t^* , needed to gain the same fraction of phase i at the current temperature, T_j , i.e.;

$$t_j = \Delta t + t_j^*$$

where t^* may, for instance, be calculated by means of JMAK model (Eq.21) as;

$$t_j^* = \left[\frac{\ln(\frac{1}{1-X_{i,j-1}})}{k(T_j)} \right]^{1/n(T_j)} \quad (54)$$

However, when cooling from the austenitic region, depending on the chemical composition of the steel, various diffusive phases may form. Obviously, during the transformation, the fraction of the

austenite reduces and the new products can only be formed from the remaining austenite phase. Therefore, to take into account this fact, the value of $X_{i,j-1}$ in Eq.54 needs to be replaced by;

$$F_{i,j-1} = \frac{X_{i,j-1}}{X_{i,j-1} + X_{\gamma,j-1}} \quad (55)$$

where $X_{\gamma,j-1}$ is the volume fraction of austenite at time step $j - 1$. Then Eq.54 takes the form;

$$t_j^* = \left[\frac{\ln(\frac{1}{1-F_{i,j-1}})}{k(T_j)} \right]^{1/n(T_j)} \quad (56)$$

Then, by application of Eq.56, the fictitious volume fraction of phase i at the end of time step j can be calculated by insertion of the modified t_j into Eq.21;

$$F_{i,j}^* = 1 - \exp(-k(T_j)t_j^{n(T_j)}) \quad (57)$$

and eventually, the volume fraction of phase i at the end of time step j can be obtain as;

$$X_{i,j} = F_{i,j}^*(X_{i,j-1} + X_{\gamma,j-1}) \quad \text{for } i = 1,2,3 \quad (58)$$

The incubation time of diffusive transformations may also be calculated by means of Eq.31, which can be approximated for the infinitesimally small time increments as

$$Q = \int_0^t \frac{d\xi}{\tau_s(T(\xi))} \approx \sum \frac{\Delta t_j}{\tau_s(T_j)} \quad (59)$$

It is assumed that the transformation starts when $Q \geq 1$. In the case of martensitic transformation, Koistinen-Marburger equation (Eq.18) can be used. Like diffusive transformation products, martensite can only be developed from the untransformed austenite. Therefore, Eq.18 needs to be modified for the multiphase systems as;

$$X_{4,j} = [1 - \exp(-0.011(M_s - T_j))] (1 - \sum X_{i,j}) \quad \text{for } i = 1,2,3 \quad (60)$$

Fig.16 shows the numerical steps in FE implementation of the heat equation incorporating the solid phase transformations.

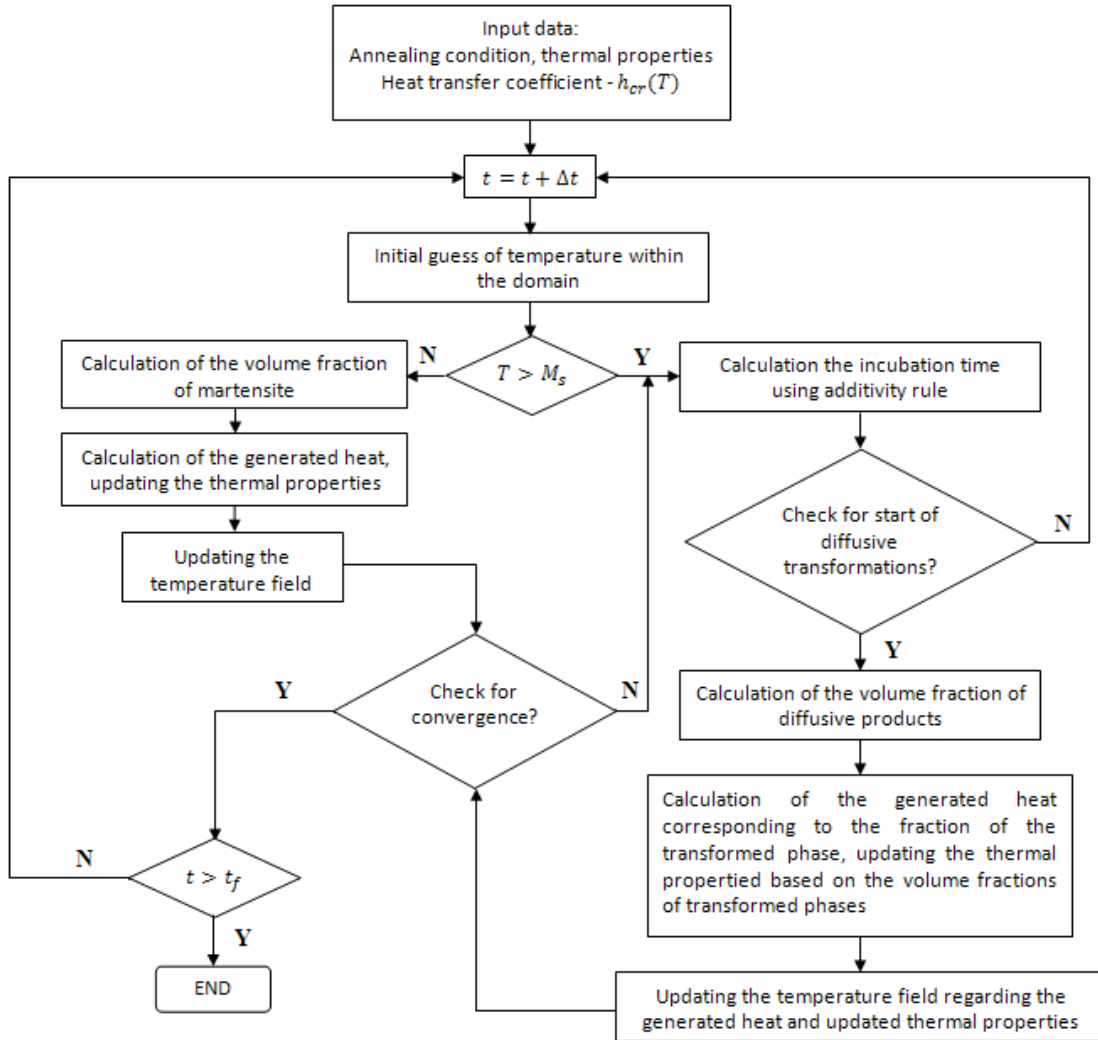


Fig.16: The algorithm applied for the numerical implementation of the heat equation incorporating the effects of phase transformation (After Nobari [27] with some modification)

2.5.4 Incorporating the effects of porosity in the developed FE model

Porosity content affects the cooling rates and final microstructure through its effects on thermal properties and kinetics of transformations. The effects of porosity on kinetics of transformations were discussed in section 2.4.5. Here, the influence of porosity on thermal properties involved in FE modeling has been studied.

Heat capacity is independent of porosity content [47], and therefore in this work, it is assumed that it only varies with temperature for each phase. On the other hand, thermal conductivity and density decrease with increasing porosity content. The density can be corrected for PM steels as;

$$\rho_s = (1 - \varepsilon)\rho_m \quad (61)$$

where ρ_s is the density of sintered component, ρ_m is the density of fully dense material and ε represents the total volume of porosity. Many relations have been proposed to relate thermal conductivity of the PM steels to the amount of porosity. Koh and Fortini [48] evaluated different relations and concluded that the best fit to experimental data for a wide range of porosity is obtained by the following equation:

$$\frac{k_s}{k_m} = \frac{1-\varepsilon}{1+\chi\varepsilon^2} \quad (62)$$

where k_m and k_s represent the thermal conductivity of the fully dense and the sintered material and χ is a constant that depends on manufacturing characteristics of porous material, contamination of material during different sintering process and accuracy of porosity-conductivity measurements. Koh and Fortini have shown that by application of $\chi = 11$, this model can be used to relate the thermal conductivity of steel powders (301 and 304L stainless steels powders) to the amount of porosity with a reasonable accuracy. In this work, the same value for χ has been considered. As can be seen in Fig.17, for the industrial level of porosity ($\approx 10\%$), the linear equation $(1 - 2.1\epsilon)$ fits the experimental data with reasonable accuracy, and therefore it can be used instead of Eq.62. The enthalpy changes of solid transformations also need to be modified as;

$$\Delta H_s (J/m^3) = (1 - \epsilon)\Delta H_m (J/m^3) \quad (63)$$

Where ΔH_s and ΔH_m are the enthalpy changes of solid transformations for sintered and fully dense components, respectively.

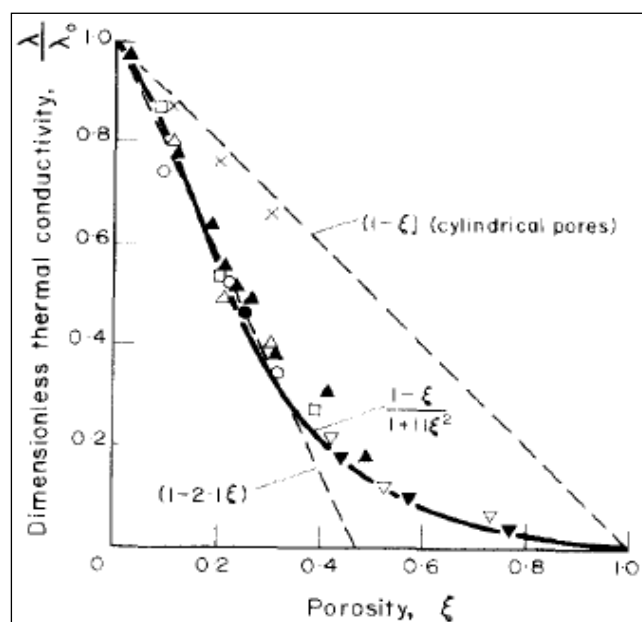


Fig.17: Comparison of experimental data and three different relations proposed for thermal conductivity of PM parts [48]

3. RESULTS

In this work, a 2D axi-symmetric FE model has been developed using MATLAB to predict the cooling response, considering the effects of nonlinear boundary conditions, latent heat generated during phase transformation and nonlinear thermal properties. By means of the established algorithm described in section 2.5.3, it is possible to simulate the effects of phase transformation when cooling from sintering temperatures. However, when implementing the numerical steps, each needs to be verified separately to ensure that the whole concept is valid. Thus, at first, an attempt has been made to verify the time and space discretization methods, irrespective of the phase transformation effects. Then, in the second step, the effects of phase transformation has also been included and the results has been verified by means of the published experimental and numerical results presented for the water quenching of a specimen with eutectoid composition. Finally, the approved algorithm has been applied to simulate the cooling response and microstructure development in PM steels.

3.1 Verification of the FE code excluding the phase transformation effects

This section deals with verification of the developed FE code while disregarding the effects of phase transformation. The aim is to ensure the accuracy in time and space discretizations and the validity of the iterative method. In this step, the Jominy test has been simulated using the current FE code, since there also exist an analytical solution for comparison if it is assumed that the effects of phase transformation are negligible, at least where the martensitic transformation takes place (i.e. close to the surface). ANSYS commercial code has also been used for comparison. Assuming that the Jominy bar can be treated as a semi-infinite plate, exposing to convective boundary condition from one side, there is a 1D analytical solution as [44];

$$\frac{T(x,t) - T_i}{T_\infty - T_i} = \operatorname{erfc}\left(\frac{x}{2\sqrt{\alpha t}}\right) - \left[\exp\left(\frac{hx}{k} + \frac{h^2\alpha t}{k^2}\right)\right] \left[\operatorname{erfc}\left(\frac{x}{2\sqrt{\alpha t}} + \frac{h\sqrt{\alpha t}}{k}\right)\right] \quad (64)$$

Therefore, the temperature at different times and locations in the bar, $T(x, t)$, can be obtained if its value is known at the previous time step. In Eq.64, T_i and T_∞ are the initial and ambient temperatures, respectively. h , k and α represent the heat transfer coefficient, thermal conductivity and thermal diffusivity and erfc is the complementary error function.

Here, for all analyses, 900°C is assumed as the initial temperature and the convection boundary condition for water quenching given in [49] is applied to the bottom edge of the model, $x = 0$. MATLAB fitting toolbox has been used to express it in a form of a polynomial;

$$h(T) = \begin{cases} 20 & T < 225^\circ\text{C} \\ -2.11 \times 10^{-9}T^4 + 3.78 \times 10^{-6}T^3 - 0.00217T^2 + 0.555T - 32.47 & 225^\circ\text{C} < T < 800^\circ\text{C} \\ 92.5 & T > 800^\circ\text{C} \end{cases}$$

Temperature dependent thermal properties of a typical low alloy steel have been used as the input for these analyses [50]. Fig.18 and Fig.19 show the temperature distribution within the bar, comparing the results obtained from the current FE code and ANSYS software. Fig.20 and Fig.21 show the comparison between the numerical results and analytical solution at the surface, $x = 0$ and at 5 mm distance from the quenched surface. As can be seen, there is a good correlation between the numerical and analytical results, approving the validity of the established FE code.

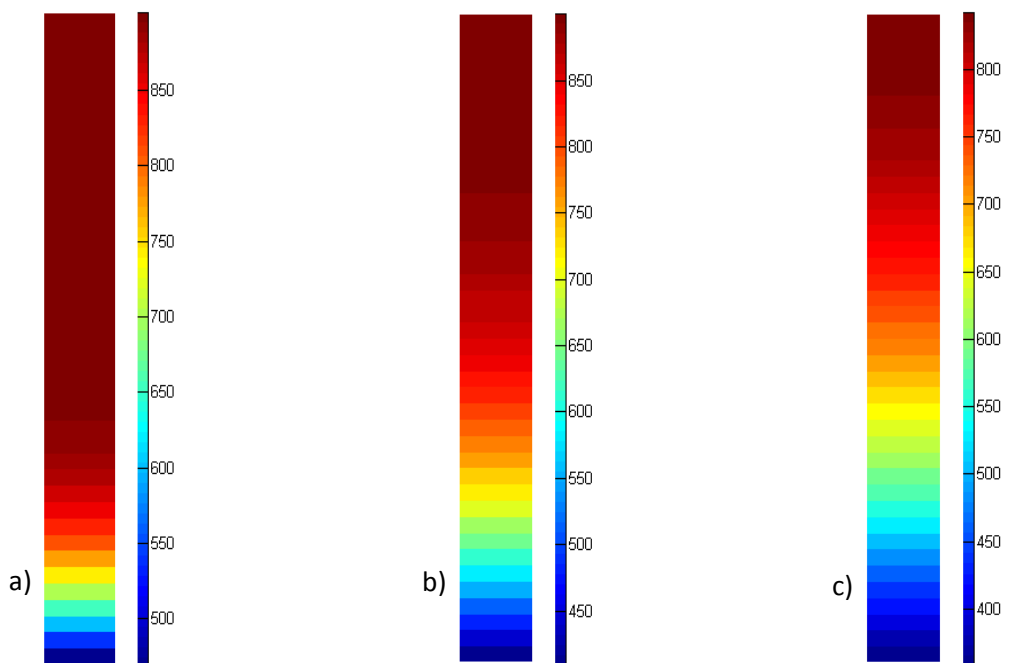


Fig.18: The Temperature distribution obtained from the MATLAB code after a:25 sec., b:100 sec., c:300 sec.

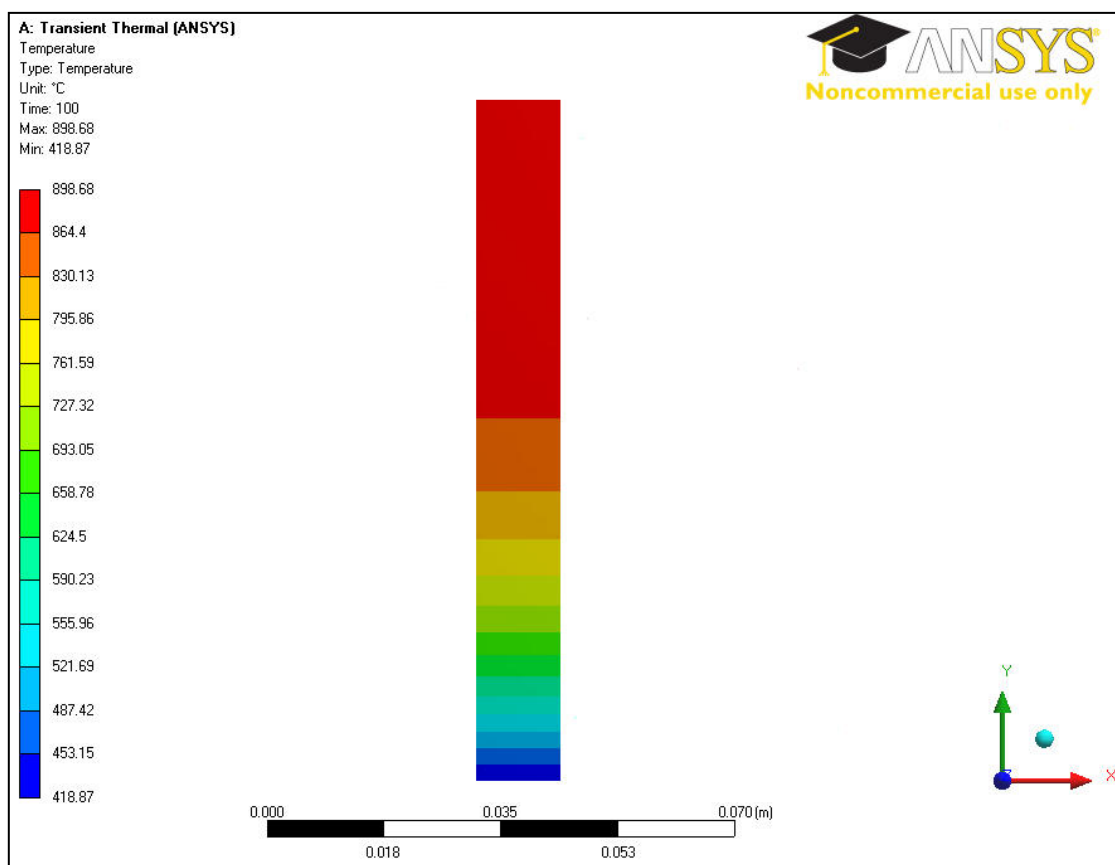


Fig.19: The Temperature distribution obtained from ANSYS after 100 sec.

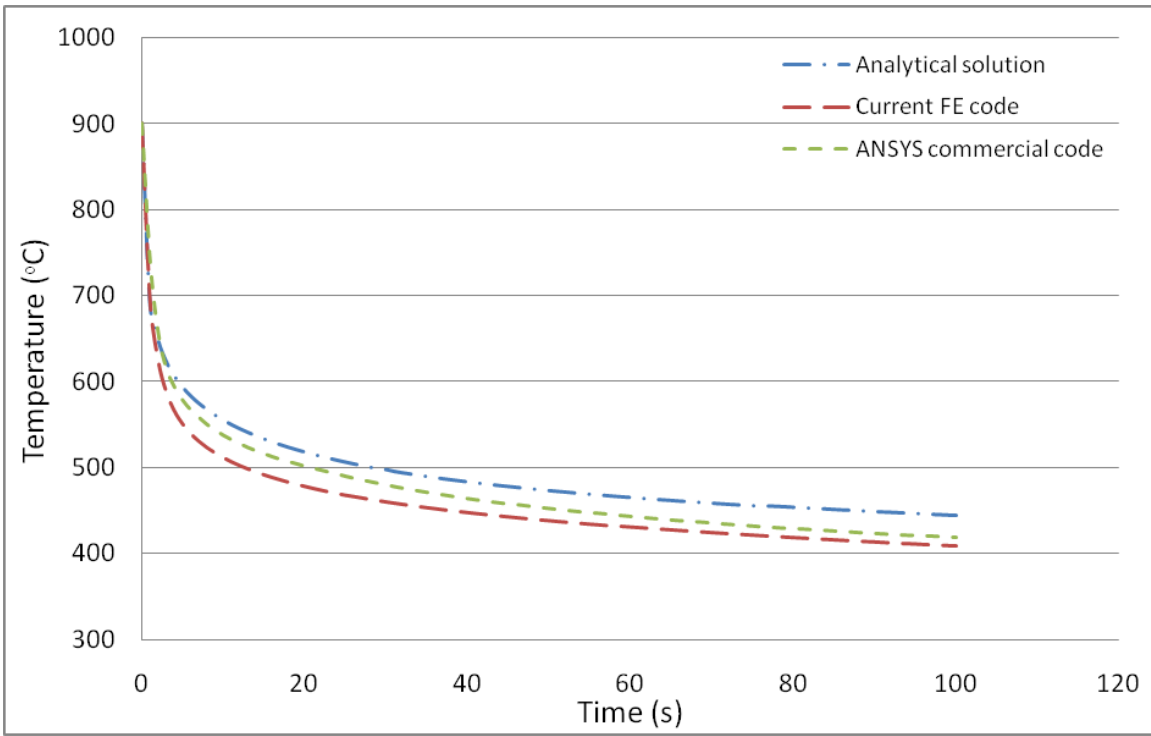


Fig.20: comparison between different tools used for simulation of cooling response of the PM steel on surface, $x=0$

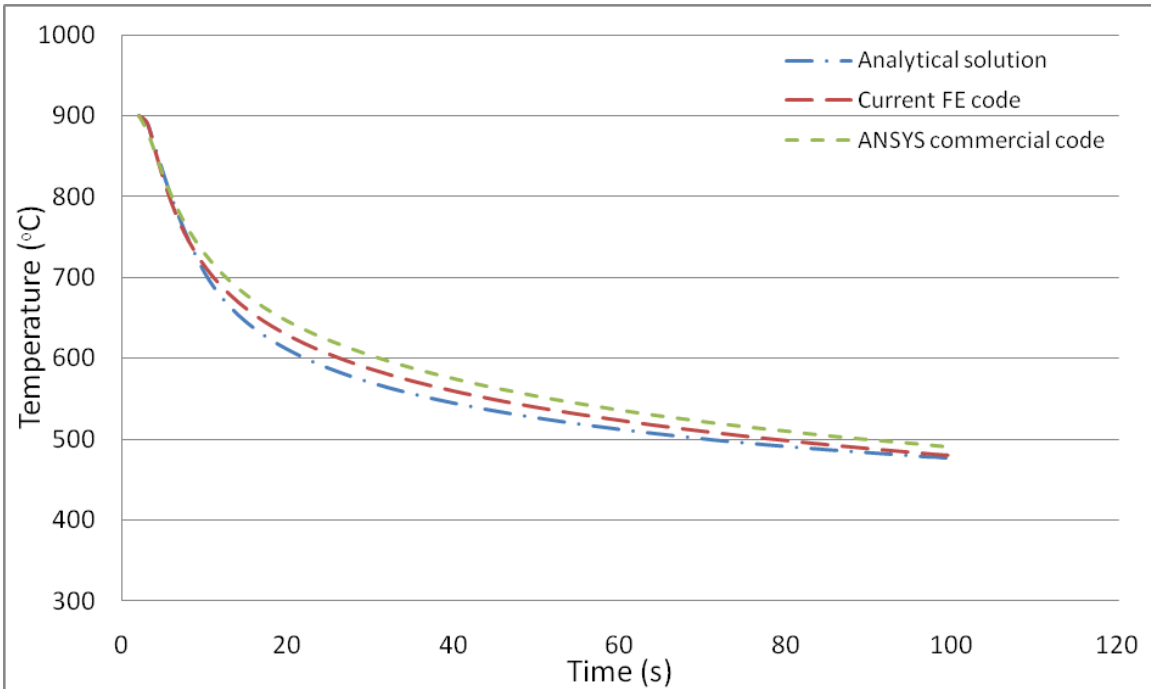


Fig.21: comparison between different tools used for simulation of cooling response of the PM steel, 5 mm from the cooling surface

3.2 Verification of the FE code including the phase transformation effects

The effects of phase transformation, in particular, the latent heat of solid transformations can be included in numerical analysis by fully implementation of the algorithm shown in Fig.16, section 2.5.3. In this step, an attempt is made to verify the established FE code with experimental and numerical results already available for solid steels. Thus, the results of the current model have been

compared with the experimental and numerical results reported in Ref.51 and Ref.52, in which similar hypothesis was established to simulate the water quenching process of a cylindrical specimen with eutectoid composition, 1080 carbon steel. Fig.22 shows the dimensions of the specimen, and the position of the holes drilled to attach the thermocouples. Due to the symmetry of the specimen, only a half of the cylinder has been modeled, to reduce the computational time. Fig.23 and Fig.24 show the TTT diagram for 1080 carbon steel and the temperature dependent convective boundary condition has been calculated using inverse iterative method [51]. The austenitizing temperature and the quenchant temperature are assumed 850°C and 22.5°C, respectively. The temperature dependent thermal properties for austenite, pearlite and martensite have also been reported in Ref.52. Similar values are used for current simulations. The following enthalpy changes for solid transformations are used in this step;

$$\Delta H_P (J/m^3) = 1.56e9 - 1.5e6 \times T(^{\circ}C)$$

$$\Delta H_M (J/m^3) = 640e6$$

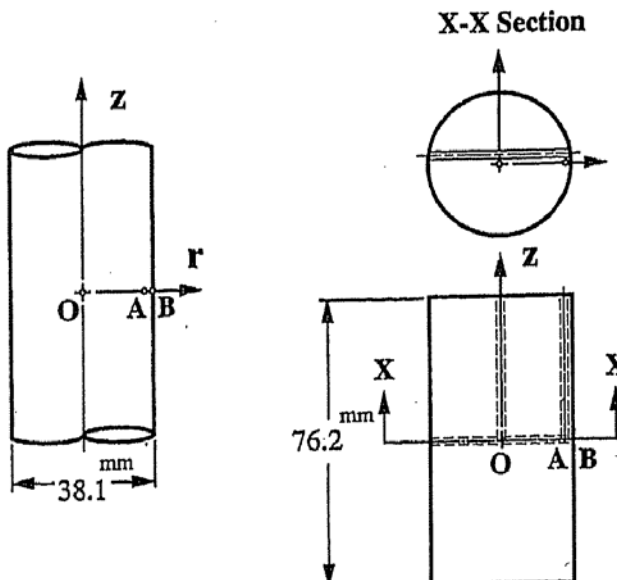


Fig.22: specimen dimensions and the position of the thermocouples [52]

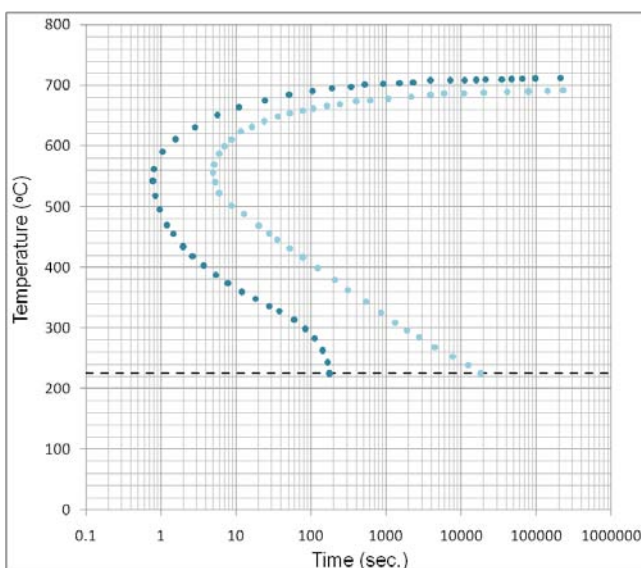


Fig.23: TTT diagram of 1080 eutectoid steel [52]

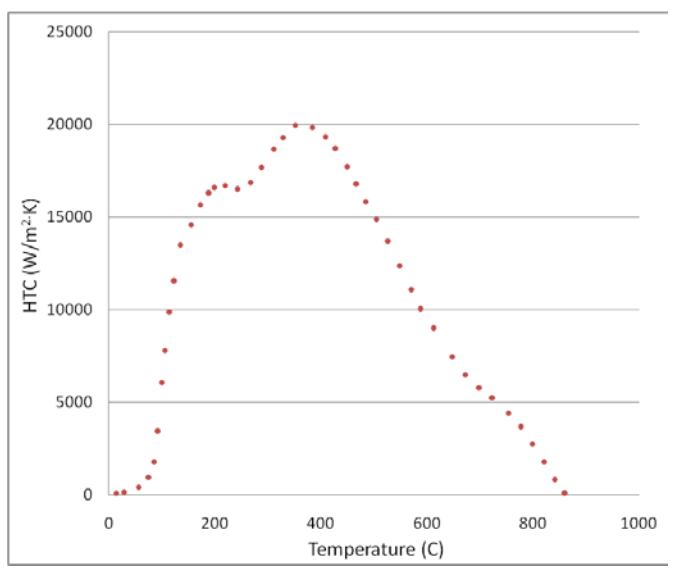


Fig.24: temperature dependent convective boundary condition [51]

Fig.25 shows the comparison between the results of the current FE simulation and the experimental and numerical results reported in Ref.52. The meshed model, which can also be seen in Fig.25, is a section from quarter of the cylinder shown in Fig.22. Points O and B are located at the center and on the surface, respectively. Fig.26 shows the comparison between cooling profiles obtained using AR and JMAK models. The distribution of temperature, martensite and pearlite phases at various times are shown in Fig.27 to Fig.29.

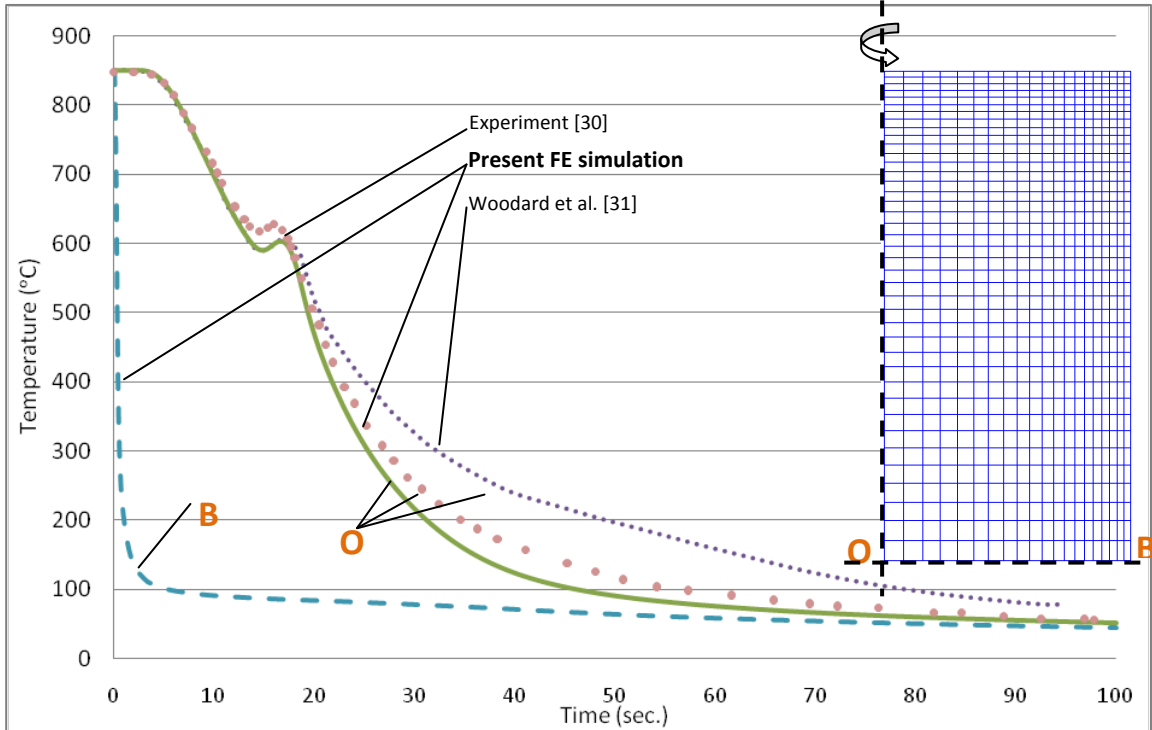


Fig.25: Temperature profile on cooling from austenitizing temperature 850C for point O and B, comparison between experimental data and present FE simulation, O: center and B: surface

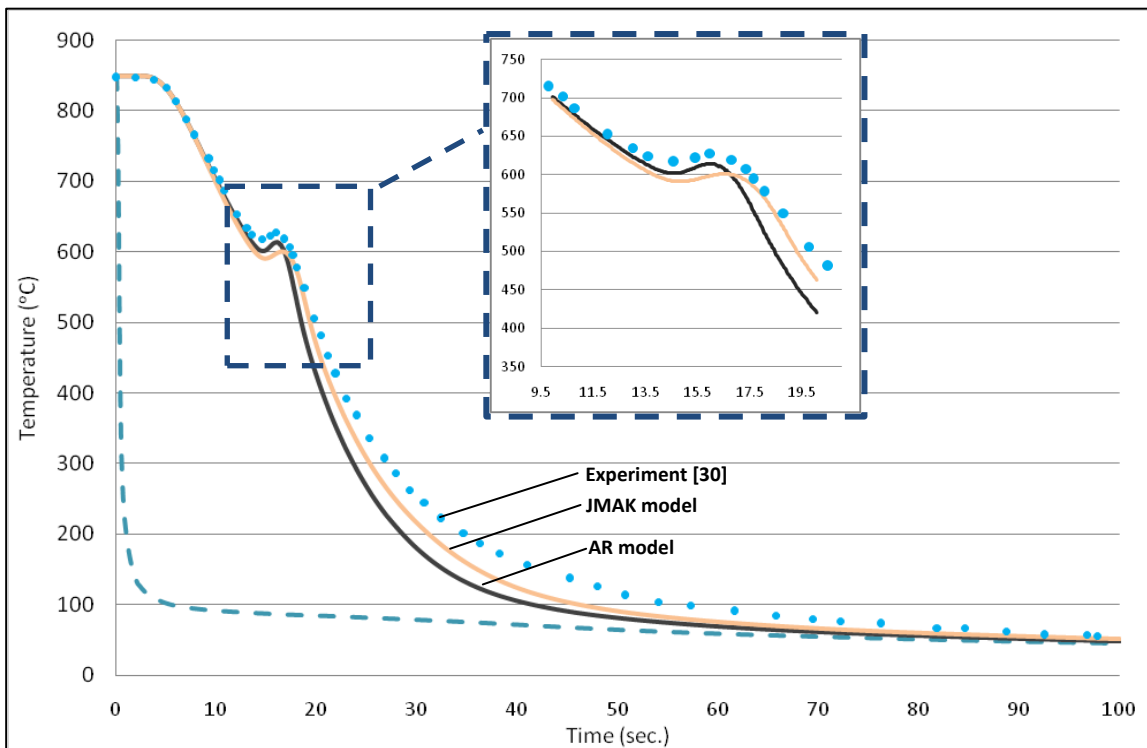


Fig.26: The comparison between AR and JMAK models

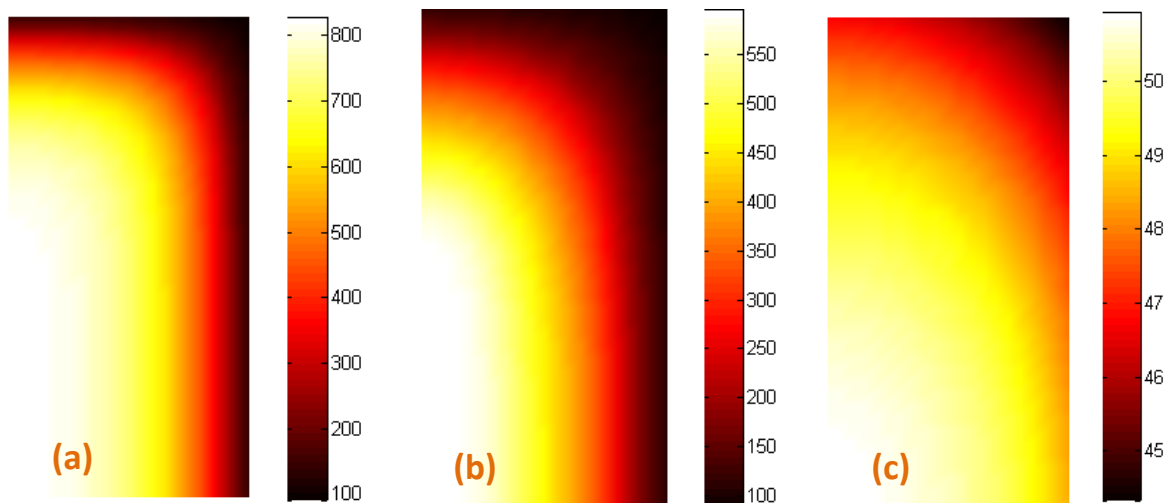


Fig.27:Temperature (°C) distribution within the cylinder after quenching a)5 sec. b)15 sec. c)100 sec.

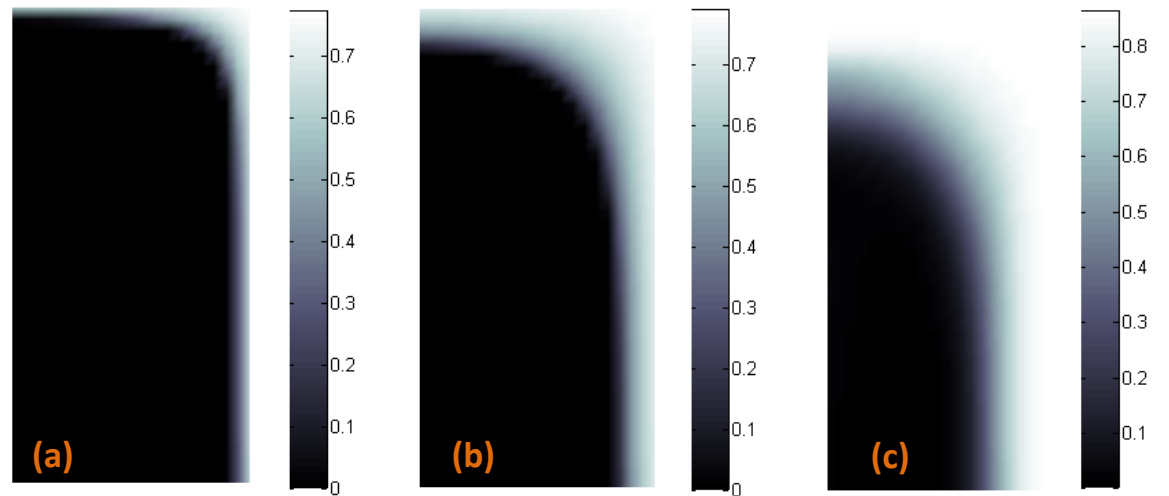


Fig.28:Martensite volume fraction after quenching a)5 sec. b)15 sec. c)100 sec.

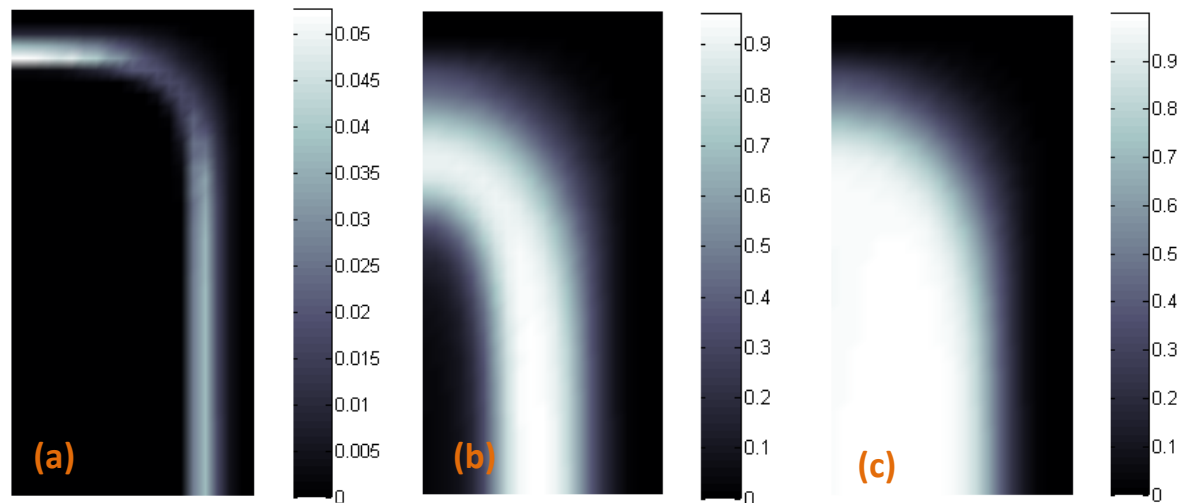


Fig.29:Pearlite volume fraction after quenching a)5 sec. b)15 sec. c)100 sec.

The distribution of the phases along the radius of the sample after 100 second cooling in water is shown in Fig.30. The comparison between the results obtained by both AR and JMAK models has also been shown in this figure.

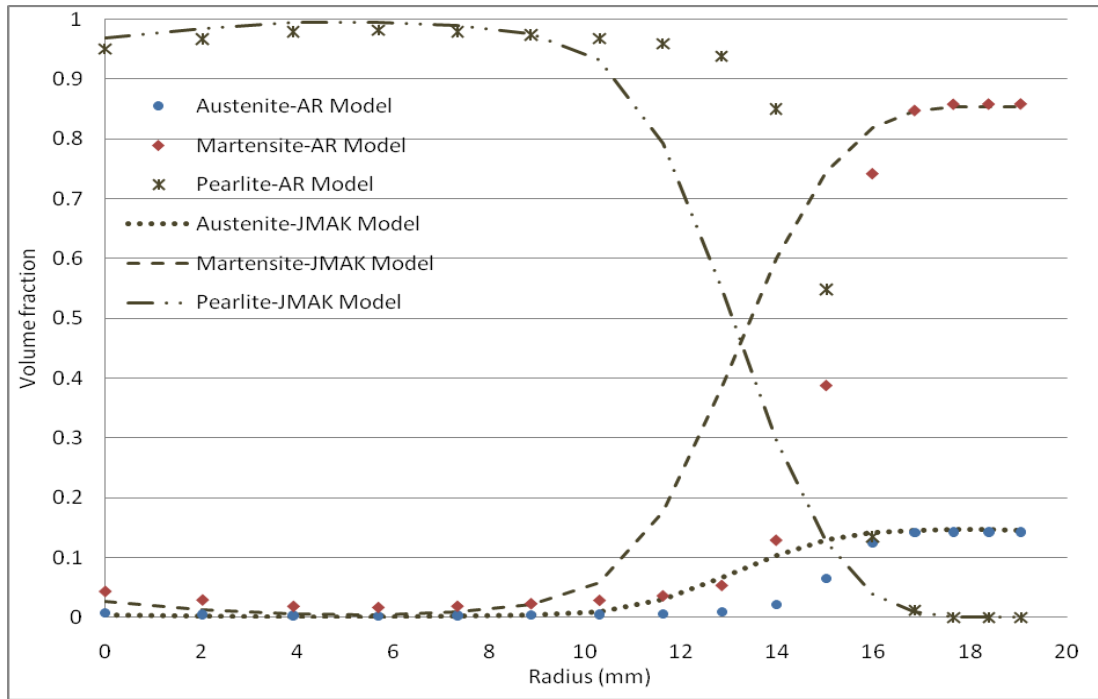


Fig.30: The distribution of different phases along the radius of the sample after 100 sec. cooling in water, comparison between AR and JMAK models

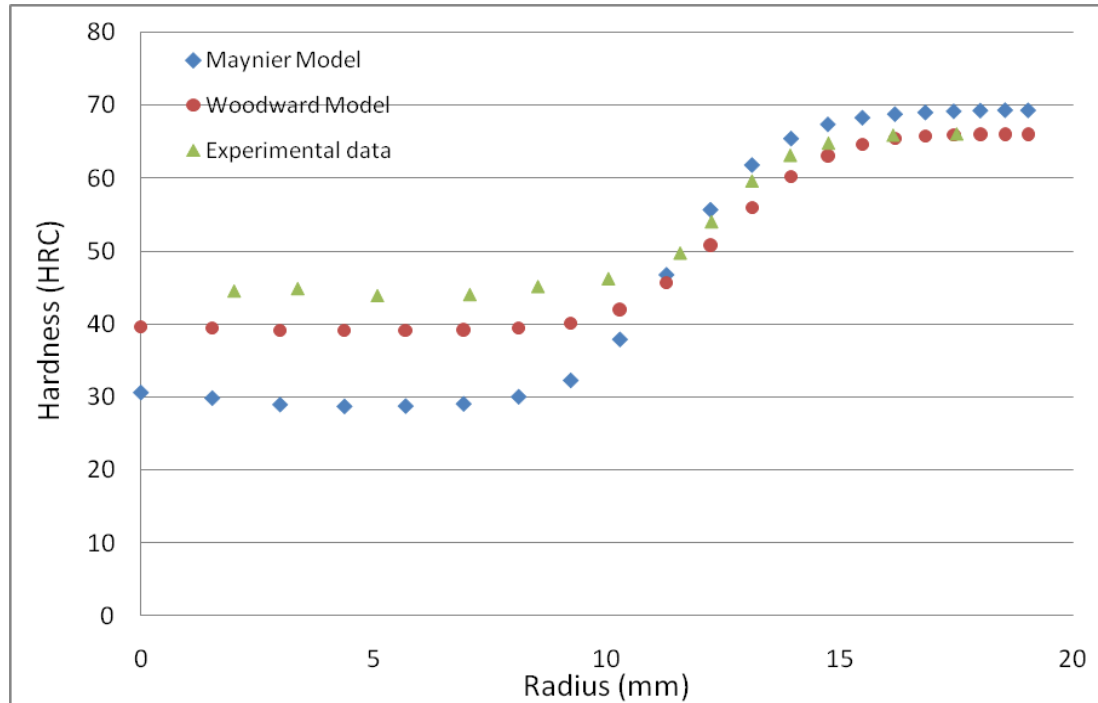


Fig.31: Distribution of hardness vs. radial distance from the center. Comparison between experimental and calculated results

The calculated and experimental hardness distribution over the radius of the specimen is shown in Fig.31. Woodard et al. [51] assumed constant hardness values for pearlite, martensite and residual austenite, regardless of cooling rates. The model developed by Maynier [53], on the other hand,

considers both the effects of cooling rates and alloying content on the hardness values for each phase. However, Fig.31 shows that the latter model cannot predict the pearlite hardness accurately. When more than two phases are transformed, linear rule of mixture is used to calculate the hardness values. It should be noted that in order to obtain the hardness distribution shown in Fig.31, JMAK model is used for kinetics of pearlitic transformation.

3.3 Cooling response in Astaloy CrL+0.6%C and Astaloy CrL+0.8%C

The same hypothesis can be applied to simulate the cooling response and microstructure development of PM steels, when the effect of porosity on kinetics of transformation and material properties is considered. In this work, only the effect of porosity on physical properties has been taken into account, due to the need for extensive experimental data to include the effects of porosity on kinetics of transformations.

The heat transfer coefficient (HTC) is calculated in such a way that the cooling rates in range 1120°C to 700°C becomes constant. However, below this temperature range, depending on the cooling rates and the kinetics of transformation, different phases may form, leading to release of latent heat of transformation. Here, an attempt is made to study the effects of heat release on the final microstructure.

Under certain circumstances, when the thermal gradient inside the specimen is negligible, the heat transfer coefficient can be determined by combining the Newton's law of cooling and Fourier's law of conduction [44];

$$h = -\frac{\rho V C_p}{A(T-T_\infty)} \frac{dT}{dt} \quad (65)$$

where V and A are the volume and the surface area of the workpiece, respectively, and T_∞ represents the ambient temperature. Biot number gives an index for the significance of thermal gradient inside a body;

$$Bi = \frac{hL}{k} \quad (66)$$

where L , h and k represent the volume to area ratio, heat transfer coefficient and thermal conductivity. For $Bi < 0.1$, the temperature gradient inside the body can be neglected, and therefore, Eq.65 can be used to calculate the heat transfer coefficients. The primarily calculations showed that the Biot number for a cylindrical specimen with 20 mm in diameter and 10 mm in length is significantly small ($Bi = 0.04$) for typical carbon steels, cooled in an environment with heat transfer coefficient as high as 500 W/m^2K , which is, in fact, 2 to 3 times higher than the actual condition within the industrial furnaces. Therefore, similar dimensions are used for FE modeling to maintain certain cooling rates unchanged during simulation of sinter hardening process when the corresponding calculated values of heat transfer coefficients are applied on the boundaries of the FE model.

JMatPro software has been used to obtain the thermal properties of a wrought steel with chemical composition similar to Astaloy CrL+0.6%C. (1.5 %Cr, 0.2 %Mo, Fe-Bal. (wt.%)). The temperature dependent specific heat capacities and thermal conductivities of different phases are shown in Table.1 and Table.2. In order to determine the values of heat transfer coefficients in range 1120 °C to 700 °C, the properties given in these tables need to be modified for a certain level of porosity. In this work, the sintering density is assumed 7 g/cm^3 , equivalent to 10% porosity.

| Phase | ρC_p (J/m^3K) | |
|------------------|---|--------------------|
| Austenite | $0.00059T^3 - 1.3809T^2 + 1916T + 3618814$ | $T < 1120^\circ C$ |
| Pearlite/Bainite | $0.00002T^4 - 0.0199T^3 + 8.2598T^2 + 1389.2666T + 3653622$ | $T < 760^\circ C$ |
| Martensite | $-0.06083T^2 + 3103.42115T + 3396258$ | $T < 300^\circ C$ |

Table.1: Temperature dependent specific heat capacity for different phases in solid steel with Astaloy CrL composition

| Phase | k ($W/m K$) | |
|------------------|---|---------------------|
| Austenite | $0.01269T + 16.6340$ | $T < 1120^{\circ}C$ |
| Pearlite/Bainite | $0.000000332T^3 - 0.00004T^2 - 0.000642T + 39.94$ | $T < 760^{\circ}C$ |
| Martensite | $0.000002263T^3 - 0.0001479T^2 + 0.00803027T + 42.5562$ | $T < 300^{\circ}C$ |

Table.2: Temperature dependent thermal conductivity for different phases in solid steel with Astaloy CrL composition

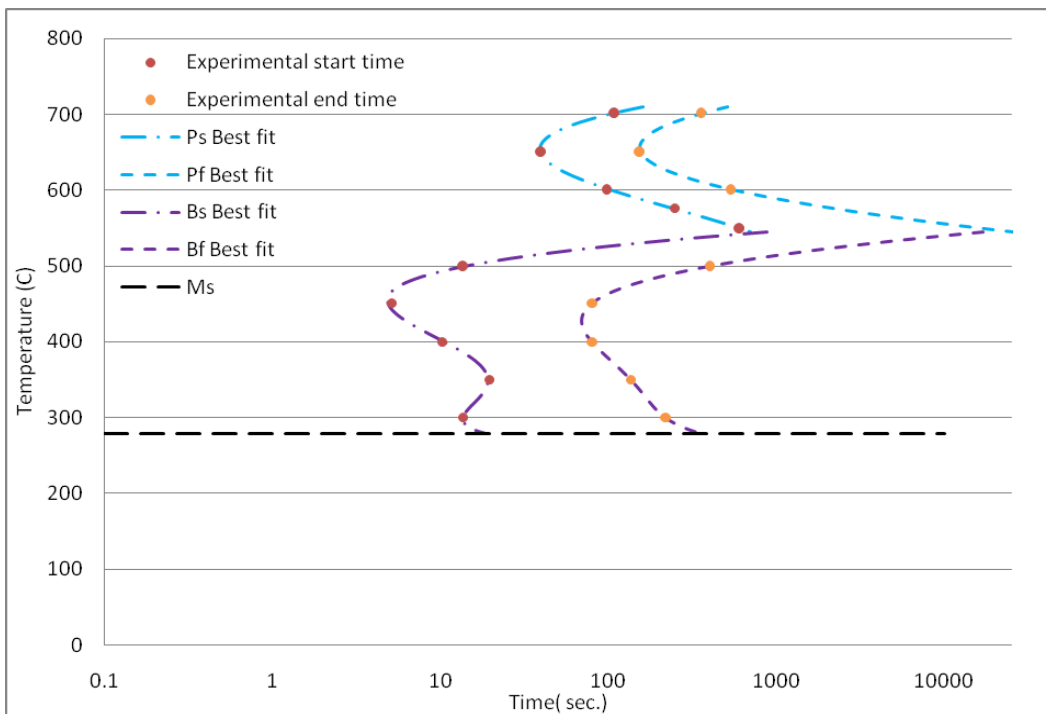


Fig.32: TTT diagram for Astaloy CrL+0.6% C

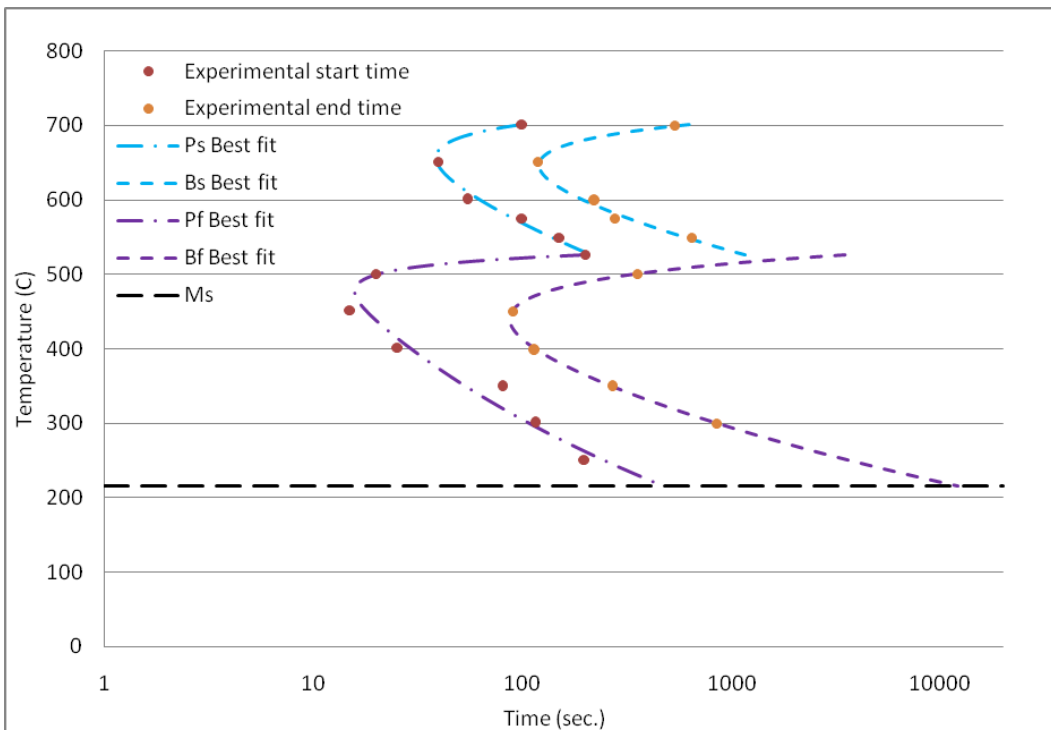


Fig.33: TTT diagram for Astaloy CrL+0.8% C

It is assumed that the enthalpy changes of solid transformations in fully dense Astaloy CrL are similar to those given in section 3.2. However, like the other material properties, the enthalpy changes have also been modified to cover the effects of porosity. Fig.32 and Fig.33 show the experimental TTT diagrams for Astaloy CrL+0.6%C and Astaloy CrL+0.8%C, respectively. The best fitted curves are also shown in these figures.

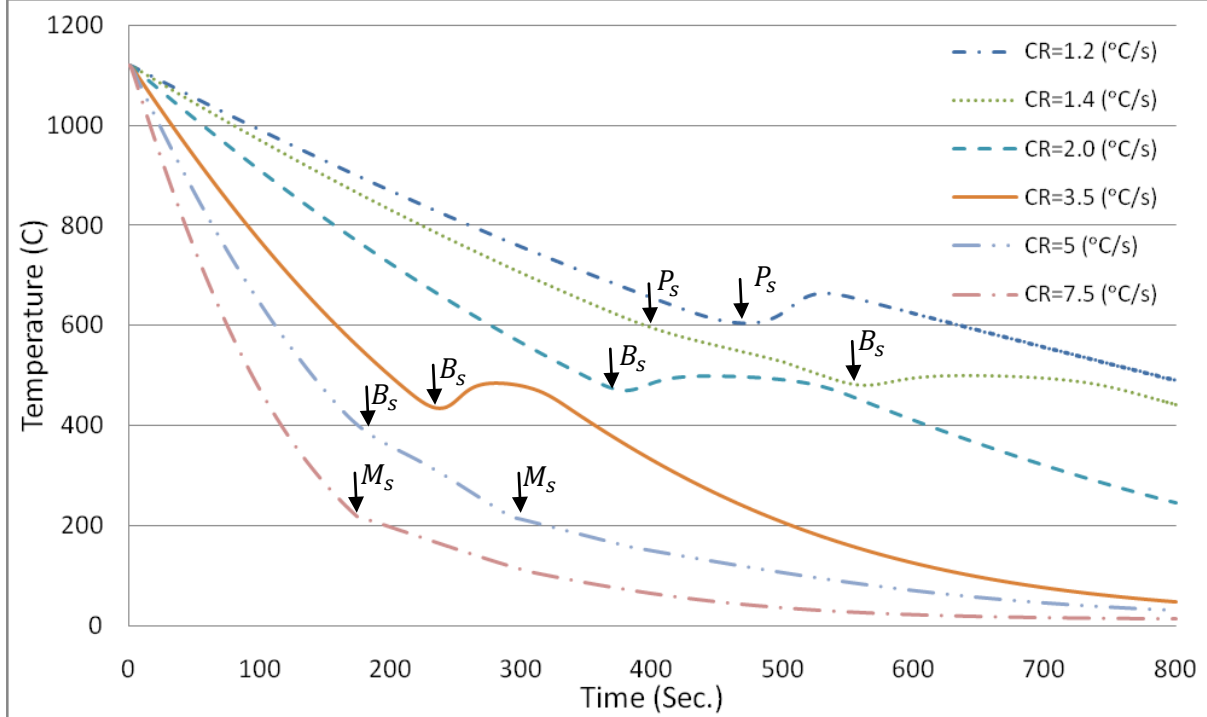


Fig.34: cooling profiles obtained for constant cooling rates in range 1120 °C-700 °C, Astaloy CrL+0.8%C, 10% porosity. CR stands for cooling rate. The arrows show the transformation start times and temperatures

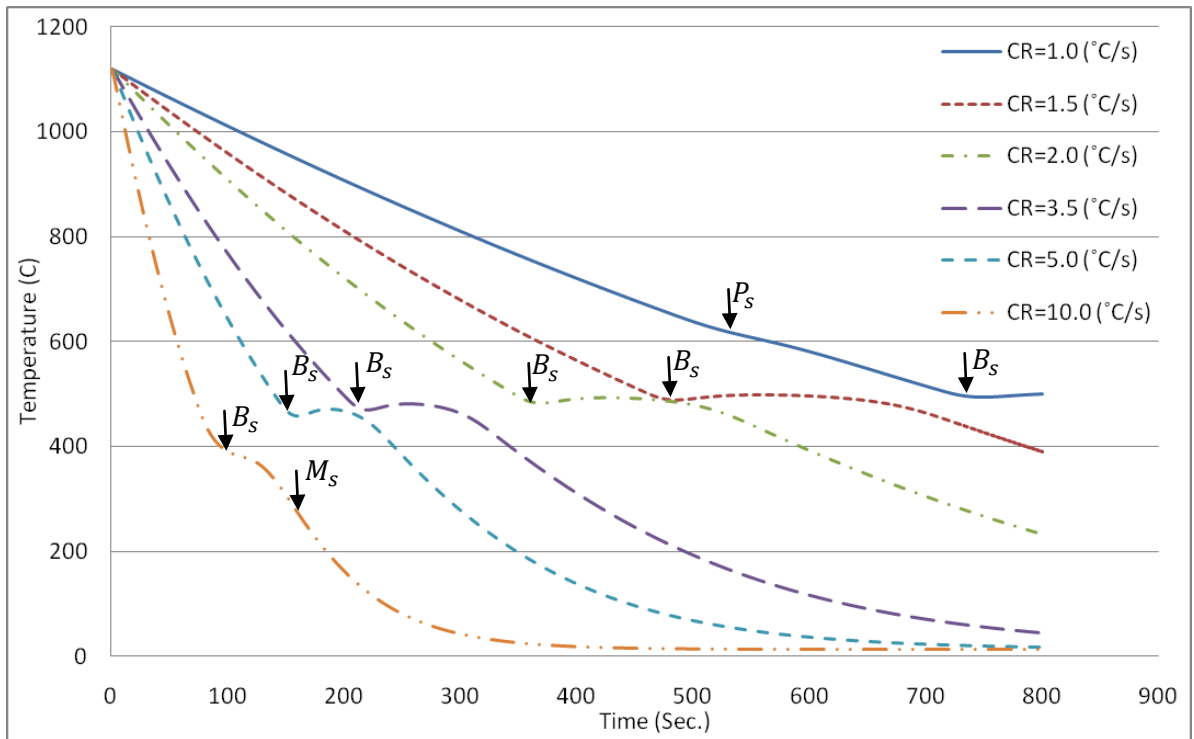


Fig.35: cooling profiles obtained for constant cooling rates in range 1120 °C- 700 °C, Astaloy CrL+0.6%C, 10% porosity. CR stands for cooling rate. The arrows show the transformation start times and temperatures

Fig.34 shows the calculated cooling profiles for Astaloy CrL+0.8%C including 10% porosity. The convective boundary conditions applied on the FE model are calculated by Eq.65 to attain constant cooling rates in range 1120 °C to 700 °C. In Fig.34, CR stands for cooling rates. The transformation start times and temperatures are also shown in this figure. The calculated cooling profiles for Astaloy CrL+0.6%C including 10% porosity is shown in Fig.35.

Fig.36 shows the simulated CCT diagram using the concept introduced by Scheil (see section 2.4.4) and the experimental TTT diagram shown in Fig.32. The experimental starting transformation times of pearlite and bainite are also shown in this figure for comparison.

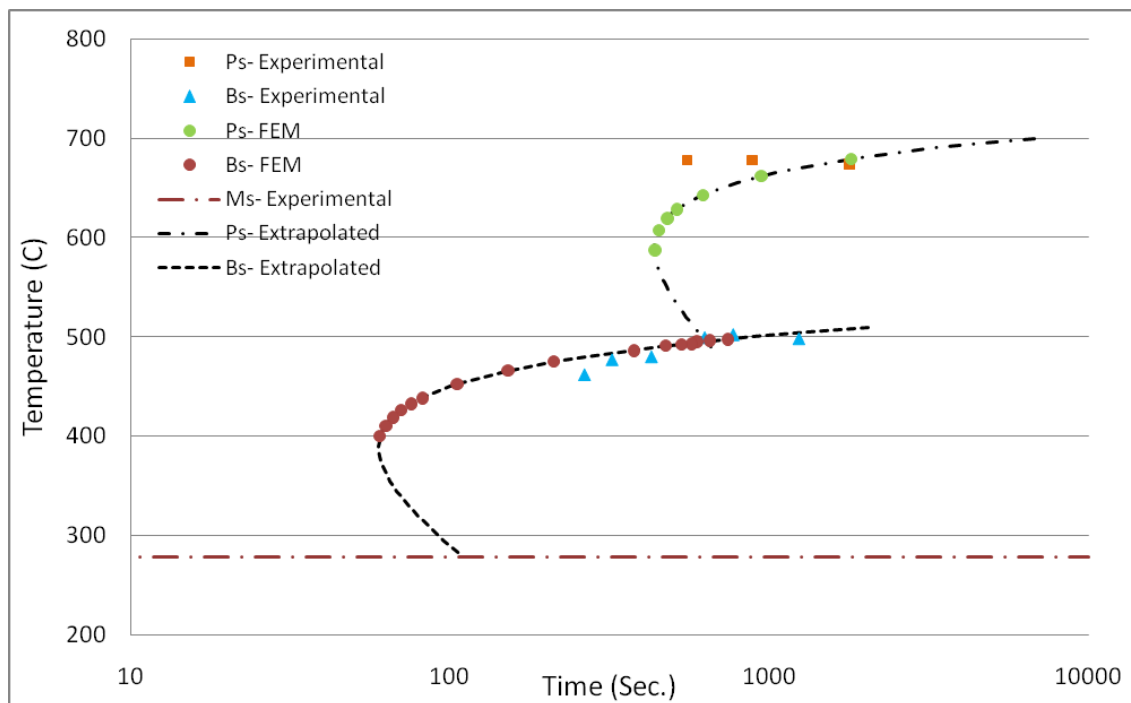


Fig.36: dilatometric and calculated CCT diagram for Astaloy CrL+0.6%C

4. DISCUSSION:

4.1 Verification routine

In section 3.1, the accuracy of the time and space discretization method was evaluated. Fig.20 and Fig.21 shows the comparison between the results obtained by the established FE code, ANSYS software and the analytical solution of the heat equation for semi-infinite plates. As can be seen in these figures, the maximum temperature difference between the results of the present model and ANSYS software are less than 5% at $x = 0$ and less than 2% at $x = 5\text{mm}$. In section 3.2, the effects of phase transformation was included. In order to ensure the accurate implementation of the numerical algorithm shown in Fig.16, the results of the current model were compared with those presented in Ref.52. As shown in Fig.25, the result of the present model is in close agreement with experimental and numerical results reported in Ref.52. The numerical results show that the present model can accurately predict the hump due to the heat release of pearlitic transformation. The difference between the numerical and experimental results is probably due to inaccuracy in thermal and physical properties of each phase, inaccuracy in boundary conditions and inconsistency between the grain size and the chemical composition of the specimen and the TTT diagram used for FE simulation. Fig.30 and Fig.31, respectively, show the distribution of the phases and the hardness values (HRC) along the symmetry axis OB, shown in Fig.25. As can be seen in Fig.31, the model proposed by Maynier [53] underestimates the hardness values of pearlite in plain carbon steels. However, the results show that the model can fairly predict the transition region between pearlite and martensite phases inside the cylinder. Knowledge of the achievable hardness for a given component size and heat treatment condition (as shown in Fig. 31) could be of great importance for designers at the early stages of the product development as well as for process engineers when deciding for the correct heat treatment procedure.

The phase distribution illustrated in Fig.30 shows that the Asutin-Rickett (AR) model predicts a faster completion for pearlitic transformation compared to the JMAK model. This can also be understood from Fig.26. The hump in the cooling profile that is obtained by means of the AR model shrinks faster, leading to a larger deviation from experimental data afterward. The difference between cooling profiles predicted by AR and JMAK models is, in fact, due to the difference in volume fractions of each phase, and its influence on the overall thermal/physical properties during cooling.

4.2 FE modeling of cooling response in Astaloy CrL PM Steel

In this work, the cooling response of Astaloy CrL with two carbon content was simulated. The TTT diagrams of these alloys are shown in Fig.37. These TTT diagrams are produced experimentally by Höganäs AB. The effect of carbon content on incubation times of pearlitic and bainitic transformation is not similar. As expected, the bainite nose is shifted to later times with increasing carbon addition, (hardenability increases with carbon addition), while the position of pearlite nose remains unchanged. This is probably due to carbon depletion at higher temperatures, or inaccuracy in microstructure analyses/dilatometric measurements. However, as can be seen in Fig.34 and Fig.35, for the industrial range of cooling rates in sinter hardening process ($2^{\circ}\text{C}/\text{s} < CR < 4^{\circ}\text{C}/\text{s}$), the final structure is generally bainitic and/or martensitic. The results of current FE simulations showed that the structure of Astaloy CrL+0.8%C is fully martensitic for cooling rates greater than $5^{\circ}\text{C}/\text{s}$, whereas according to the simulated CCT diagram shown in Fig.36, for Astaloy CrL+0.6%C a fully martensitic microstructure is acquired by applying cooling rates higher than $15^{\circ}\text{C}/\text{s}$. As can be seen in Fig.36, the simulated CCT diagram by application of Scheil's principle is in good agreement with dilatometric data.

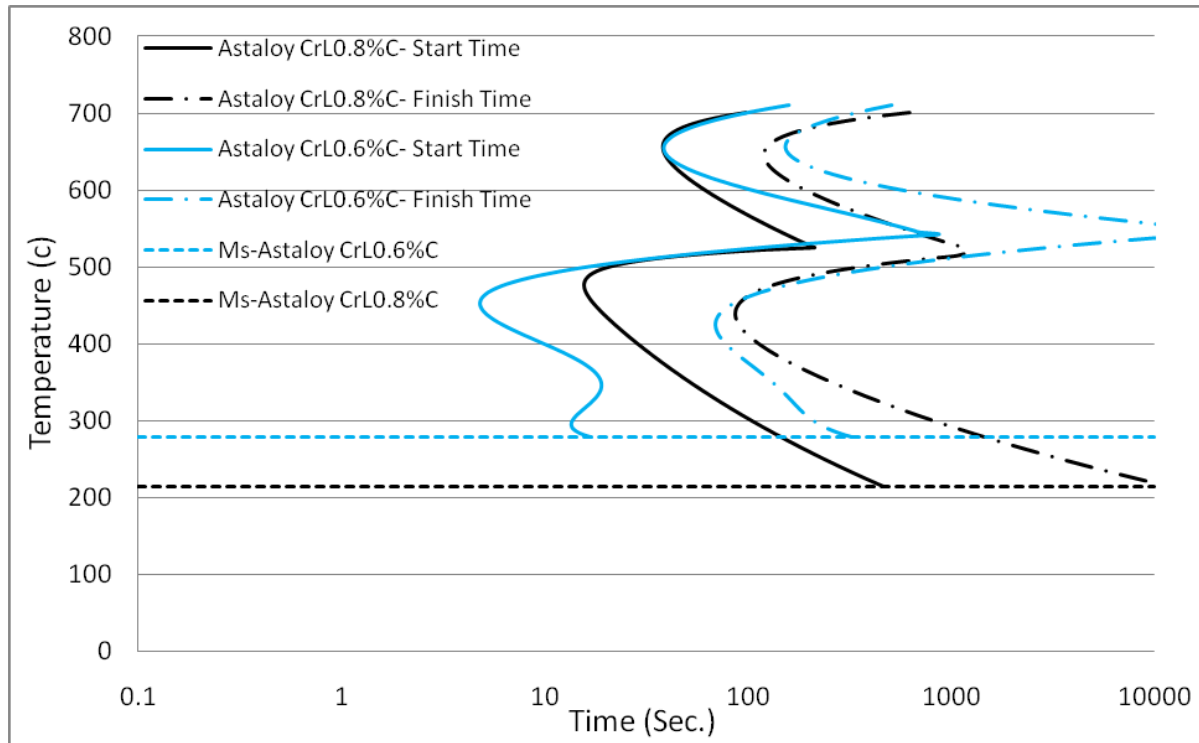


Fig.37: TTT diagrams of Astaloy CrL+0.6%C and Astaloy CrL+0.8% C ($\rho \approx 7 \text{ g/cm}^3$)

4.3 Considerations for PM steels

In sections 2.4.5 and 2.5.4, the effects of porosity on kinetics of transformation and physical properties were discussed in detail. It is shown that the porosity may affect the kinetics of diffusive transformation by increasing the number of potential sites for nucleation and by providing the additional diffusion path inside the material [38]. In addition, the dilatometric analyses conducted by Warke et al. [39] showed that porosity affects the kinetics of martensitic transformation in PM steels; M_s increases with increasing the porosity content. It is speculated that this increase may be due to the carbon loss during sintering process and/or assisting effects of pore free surfaces on reducing the energy barrier necessary for martensitic transformations. Porosity also affects the cooling behavior by reducing the density and thermal conductivity according to Eq.61 and Eq.62. It is known that in PM steels, the cooling rates increases with increasing the porosity content [50]. Hence, in order to simulate the cooling response and microstructure development in PM steels, the material properties and transformation diagrams are to be modified for a specific level of porosity. Hatami et al. [50] showed that the influence of porosity on the cooling response can be simulated by application of Eq.61 and Eq.62. However, in order to take into account the effects of porosity on transformation kinetics, the models described in section 2.4.1 and section 2.4.4 are to be corrected for porosity. An obvious influence of porosity is to shorten the incubation period of diffusional transformations; which means that in PM steels the TTT diagram shifts to the earlier times with increasing the porosity. Supposing that the TTT diagrams for a specific level of porosity is available, the incubation time of transformation for a material with different porosity content can be estimated by modifying Eq.31 (see section 2.4.4);

$$\int_0^t \frac{d\xi}{(\frac{\varepsilon_{TTT}}{\varepsilon})^q \tau_s(T(\xi))} = 1 \quad (67)$$

where τ_s is the starting time of transformation at a given temperature and level of porosity. ε_{TTT} is the porosity content of the sample which the TTT diagram is produced for, and ε is the porosity content of the component under study. q is an exponent which is different for ferrite, pearlite and

bainite transformations due to the different effects of porosity on nucleation process. The probable effects of porosity on growth mechanisms can also be taken into account by modifying the JMAK model (Eq.21);

$$X = 1 - \exp(-k(T)\left(\frac{\varepsilon}{\varepsilon_{TTT}}\right)^p t^n) \quad (68)$$

where p is an exponent that varies for ferrite, pearlite and bainite transformations due to the different effects of porosity on kinetics of transformations. In accordance with the study conducted by Warke et al. [39], the correction parameters in Eq.68 increases with increasing porosity content, leading to a faster growth mechanism for less dense materials. In order to determine q and p parameters in Eq.67 and Eq.68, the numerical results should be compared with experimental data provided for different level of porosity, cooled under controlled condition.

Based on the study conducted by Warke et al. [39], Semel and Lados [43] suggested that the M_s in PM steels increases by 2.3°C per 1% porosity. The equation proposed by Koistinen and Marburger (see section 2.3.2.5) can be used to obtain the volume fraction of the martensite in PM steels.

5. CONCLUSIONS:

1. A 2D axi-symmetric FE model has been developed using MATLAB software, which has a practical use for many components with symmetric axis, such as rings.
2. The accuracy of the time and space discretization method was verified using a reliable commercial code, ANSYS.
3. The latent heat of phase transformation is taken into account in the developed model.
4. The simulation results were verified by comparing the results of the present model with the experimental and numerical results reported in previous studies.
5. The established FE code can be used to simulate different heat treating processes such as oil quenching, sinter hardening, etc.
6. A comparative study showed that the model can be applied to simulate the cooling response in PM steels.
7. The simulated CCT diagram for Astaloy CrL+0.6%C is in close agreement with dilatometric measurements.
8. A model is proposed to take into account the effects of porosity on transformation kinetics. However, to determine the parameters of the model, the numerical results should be compared with experimental cooling profiles measured for specimens with different level of porosity, cooled under controlled conditions.

6. ACKNOWLEDGMENT

I would like to thank Professor Lars Nyborg, my examiner, and Sepehr Hatami, my supervisor, for their kind supports and guidance throughout this work.

I would also like to thank Dr. Eduard Hryha and my friend Seshendra Karamchedu for a number of useful comments and Höganäs AB for providing us with the technical data required for this work.

Last but not least, I would like to thank my family, teachers and friends who have been a constant source of encouragement for me during my studies.

7. REFERENCES:

1. Totten, G. E., 2007. Steel Heat treatment, vol. 1: Metallurgy and Technologies, CRC press
2. James, W. B., 1998. What is sinter-hardening?, International Conference on Powder Metallurgy & Particulate Materials, Las Vegas, USA
3. Semel, F. J., 2000. Method of making powder metallurgical compositions, US6068813
4. MPIF Standard 35, 2009. Materials Standards for PM Structural Parts. Metal Powder Industries Federation
5. Vander Voort, G. F., 1991. Atlas of time-temperature diagrams for irons and steels, ASM international
6. Bhadeshia, H. K. D. H., Honeycombe, R. W. K., 2006. Steels-microstructure and Properties, third ed. Butterworth-Heinemann
7. Krauss, G., 2006. Steels-Processing, Structure, and Performance, 2005 ed. ASM International, Ohio
8. Kaufman, L., Cohen, M., Thermodynamics and kinetics of martensitic transformations, Progress in Metal Physics, vol. 7, pp. 165-246
9. Fisher, J. C., Hollomon, J. H., Turnbull, D., 1949. Kinetics of the austenite to martensite transformation, Metals Transactions, vol. 185, pp. 691-700
10. Nishiyama, Z., 1978. Martensitic transformation, Academic press
11. Ghosh, G., Olson, G. B., 1994. Kinetics of fcc to bcc heterogeneous martensitic nucleation- I. The critical deriving force for athermal nucleation, Acta Metall. Mater., vol. 42, pp. 3361-3370
12. Cool, T., Bhadeshia, H. K. D. H., 1996. Prediction of martensite start temperature of power plant steels, Materials Science and Technology, vol. 12, pp. 40- 44
13. Sourmail, T., Garcia Mateo, C., 2005. Critical assessment of models for predicting the Ms temperature of steels, Computational Materials Science, vol. 34, pp. 323-334
14. Brofman , P. J., Ansell, G. S., 1983. On the effect of fine grain size on the Ms temperature in Fe-27Ni-0.025C alloys, Metallurgical and Materials Transactions A, vol. 14, pp. 1929-1931
15. Capdevila, C., Caballero, F. G., Garcia de Andres, C., 2003. Analysis of effect of alloying elements on martensite start temperature of steels, Materials Science and Technology, vol. 19, pp.581-586
16. Guimaraes, J.R.C., Gomes, J.C., 1978. A metallographic study of the influence of the austenite grain size on martensite kinetics, Acta Metallurgica, vol. 26, pp. 1591-1596
17. Garcia-Junceda, A., Capdevila, C., Caballero, F.G., Garcia de Andres, C., 2008. Dependence of martensite start temperature on fine austenite grain size, Scripta Materialia, vol. 58, pp. 134-137
18. Dieter, G. E., 1988. Mechanical Metallurgy, McGraw-Hill Book company
19. Yang, H. S., Bhadeshia, H.K.D.H., 2009. Austenite grain size and martensite start temperature, Scripta Materialia, vol. 60, pp. 493-495
20. Lee, S. J., Lee Y. K., 2008. Finite element simulation of quench distortion in a low-alloy steel incorporating transformation kinetics, Acta Materialia, vol. 56, pp. 1482–1490
21. Grujicic, M., Dang, P., 1995. Computer simulation of martensite transformation in Fe-Ni face-centered cubic alloys, Materials Science and Engineering A, vol. 201. Pp. 194-204
22. Koistinen, D.P., Marburger, R.E., 1959. A general equation prescribing the extent of the austenite-martensite transformation in pure iron-carbon alloys and plain carbon steels, Acta Metallurgica, vol. 7, pp. 59-60
23. Bhadeshia, H. K. D. H., 2001. Bainite in Steels, 2nd ed. Institute of Materials, Minerals and Mining
24. Porter, D.A., Easterling, K.A., 2004. Phase transformation in metals and alloys, 2nd ed. CRC press
25. Matsuzaki, A., Bhadeshia, H. K. D. H., 1999. Effect of austenite grain size and bainite morphology on overall kinetics of bainite transformation in steels, Materials Science and Technology, vol. 15, pp. 518-522
26. Christian, J. W., 1965. The theory of transformations in metals and alloys, Pergamon press
27. Nobari, A. H., Serajzadeh, S., 2008. A study on microstructural changes and mechanical properties in steel rods subjected to uniform and non-uniform cooling layout using a finite element analysis, IMechE Part B: J. Engineering Manufacture, vol. 222 , pp.1639-1649
28. Serajzadeh, S., Karimi Taheri, A., 2004. A study on austenite decomposition during continuous cooling of a low carbon steel, Materials and Design, vol. 25, pp. 673-679

29. Tehler, M., 2009. Modeling phase transformations and volume changes during cooling of case hardening steels, licentiate thesis, Materials science and Engineering, Stockholm
30. Starink, M. J., 1997. Kinetics of the decomposition of austenite at constant temperature, *Journal of Material Science*, vol. 32, pp. 397-415
31. Kirkaldy, J. S., Venugopalan, D., 1983. Prediction of microstructure and hardenability in low alloy steels, Cited in Marde, A. R., Goldstein, J. I., ed. *Phase Transformations in Ferrous Alloys*, AIME, New York, NY, pp. 128-48
32. Rohde, J., Jeppsson, A., 2000. Literature review of heat treatment simulations with respect to phase transformation, residual stresses and distortion, *Scandinavian Journal of Metallurgy*, vol. 29, pp. 47-62
33. Lusk, M., Jou, H. J., 1997. On the rule of additivity in phase transformation kinetics, *Metallurgical and Materials Transactions A*, vol. 28, pp. 287-291
34. Hawbolt, E. B., Chau, B., Brimacombe, J. K., 1983. Kinetics of Austenite-pearlite transformation in eutectoid carbon steel, *Metallurgical transactions A*, vol. 14, pp. 1803-1815
35. Zhu, Y. T., Lowe, T. C., Asaro, R. J., 1997. Assessment of the theoretical basis of the Rule of Additivity for the nucleation incubation time during continuous cooling, *American Institute of Physics*, vol.82, pp.1129-1137
36. Dlapka, M., Strobl, S., Danninger, H., Gierl, C., Austenite grain size in sinter hardened powder metallurgy steels, in press
37. Liu, Y., Patterson, B. P., 1993. Grain growth inhibition by porosity, *Acta Metallurgica et Materialia*, vol. 41, pp. 2651-2656
38. Warke, V. S., Sisson Jr., R. D., Makhlof, M. M., 2009. The effect of porosity on the austenite to bainite transformation in powder metallurgy steels, *Journal of Materials Research*, vol. 24, pp. 3213-3219
39. Warke, V. S., 2008. Predicting the Response of Powder Metallurgy Steel Components to Heat Treatment, PhD thesis, Worcester Polytechnic Institute
40. Gurevich, Y. G., Rakhmanov, V. I., Pozhidaev, Y. I., 1979. Structural transformation and mechanical properties of sintered alloy steels, *Powder Metallurgy and Metal Ceramics*, vol. 18, pp. 407-410
41. Gurevich, Y. G., Rakhmanov, V. I., Pan' shin, I. F., 1986. Effect of composition and porosity on the hardenability and hardness penetration of structural powder steels *Powder Metallurgy and Metal Ceramics*, vol. 25, pp. 70-73
42. Antsiferov, V. M., Grevnov, L. M., Perel'man, O. M., 1992. Isothermal decomposition of the austenite of PM steels alloyed with chromium and molybdenum, *Metal Science and Heat Treatment*, vol. 34, pp. 527-533
43. Semel, F. J., Lados, D. A., 2009. Simulated effects of martensite start temperature, thermal conductivity and pore content on end quench cooling rate, *Powder Metallurgy*, vol. 52, pp. 282- 290
44. Holman, J. P., 1986. Heat transfer, sixth ed., McGraw-Hill: Singapore
45. Zienkiewicz O. C., Taylor L. R., 1989. The finite element method, Vol.1, 4th ed., McGraw-Hill: New York
46. Carbone, P., Palazzo, G. S., Pasquino, R., 2010. Finite element analysis of the steel quenching process: Temperature field and solid-solid phase change, *Computers and Mathematics with Application*, vol. 59, pp. 585-594
47. Saritas, S., Doherty, R.D., Lawley, A., 2001. Effect of Porosity on Thermal Diffusivity and Hardenability of PM Steels, *PM2001. EPMA*, Niece, pp. 257-265
48. Koh, J.C.Y., Fortini, A., 1973. Prediction of Thermal Conductivity and Electrical Resistivity of Porous Metallic Materials, *International Journal of Heat and Mass Transfer*, vol. 16, pp. 2013-2021
49. Bocchini, G.F., Baggio, A., Gerosa, R., Rivolta, B., Silva, G., 2004. Cooling rates of P/M steels, *International Journal of Powder Metallurgy*, vol. 40, pp. 57-65
50. Hatami, S., Malakizadi, A., Nyborg, L., Wallin, D., 2010. Critical aspects of sinter-hardening of prealloyed Cr-Mo steel, *Journal of Materials Processing Technology*, vol. 210, pp. 1180-1189
51. Woodard, P. R., Chandrasekar, S., Yang, H. T. Y., 1999. Analysis of Temperature and Microstructure in the Quenching of Steel Cylinders, *Metallurgical and Materials Transaction B*, vol. 30, pp. 815-822

52. Wang, K. F., Chandrasekar, S., Yang, H. T. Y., 1997. Experimental and Computational Study of the Quenching of Carbon Steel, *Journal of Manufacturing Science and Engineering*, vol. 119, pp. 257-265
53. Maynier, P., Dollet, J., Bastien, P., 1978. Prediction of microstructure via empirical formulas based on CCT diagrams Hardenability Concepts with Application to Steel, ed. Doane, D. V., Kirkaldy, J. S. (NY: AIME), pp. 163–176